

Determining the main-sequence mass of Type II supernova progenitors

Luc Dessart^{1*}, Eli Livne², and Roni Waldman²

¹ *Laboratoire d'Astrophysique de Marseille, Université de Provence, CNRS, 38 rue Frédéric Joliot-Curie, F-13388 Marseille Cedex 13, France*

² *Racah Institute of Physics, The Hebrew University, Jerusalem, Israel*

Accepted . Received

ABSTRACT

We present radiation-hydrodynamics simulations of core-collapse supernova (SN) explosions, artificially generated by driving a piston at the base of the envelope of a rotating or non-rotating red-supergiant progenitor star. We search for trends in ejecta kinematics in the resulting Type II-Plateau (II-P) SN, exploring dependencies with explosion energy and pre-SN stellar-evolution model.

We recover the trivial result that larger explosion energies yield larger ejecta velocities in a given progenitor. However, we emphasise that for a *given* explosion energy, the increasing helium-core mass with main-sequence mass of such Type II-P SN progenitors leads to ejection of core-embedded oxygen-rich material at larger velocities. We find that the photospheric velocity at 15 d after shock breakout is a good and simple indicator of the explosion energy in our selected set of pre-SN models. This measurement, combined with the width of the nebular-phase OI 6303–6363 Å line, can be used to place an upper-limit on the progenitor main-sequence mass. Using the results from our simulations, we find that the current, but remarkably scant, late-time spectra of Type II-P SNe support progenitor main-sequence masses inferior to $\sim 20 M_{\odot}$, and thus, corroborate the inferences based on the direct, but difficult, progenitor identification in pre-explosion images. The narrow width of OI 6303–6363 Å in Type II-P SNe with nebular spectra does not support high-mass progenitors in the range 25–30 M_{\odot} .

Combined with quantitative spectroscopic modelling, such diagnostics offer a means to constrain the main-sequence mass of the progenitor, the mass fraction of the core ejected, and thus, the mass of the compact remnant formed.

Key words: radiation hydrodynamics – stars: atmospheres – stars: supernovae – stars: transients

1 INTRODUCTION

Understanding how and which massive stars end their lives in a successful core-collapse SN explosion is still subject to large uncertainties today. Various mechanisms have been proposed, all invoking the gravitational, and sometimes rotational, energy of the collapsed core and infalling mantle. The hot proto-neutron star (PNS) that forms at core bounce releases on a timescale of ~ 10 s on the order of 100 B ($1 \text{ B} \equiv 10^{51} \text{ erg}$) of energy in the form of neutrinos. A neutrino-driven explosion hinges on the successful absorption of a few percent of this neutrino energy behind the shock (see, e.g., Herant et al. 1994). This must occur prior to black-hole formation, and thus within a few seconds at most of core bounce. This does not seem to occur *robustly* in any of the one- or two-dimensional radiation-hydrodynamics simulations performed so far with sophisticated neutrino transport and microphysics, although the latest

simulations look promising (Marek & Janka 2009). Burrows et al. (2006, but see Weinberg & Quataert 2008 and Marek & Janka 2009) proposed that if such a neutrino-driven explosion fails within a second of core bounce, the stalled shock may instead be energised by the acoustic power associated with gravity-mode oscillations of the PNS. In such simulations, core oscillations could power an explosion over a wide range of massive-star progenitors, as obtained for objects with a main-sequence mass between 11 and 25 M_{\odot} by Burrows et al. (2007b). Finally, provided the progenitor star possesses a very fast-rotating core at the onset of collapse (typically with a 1-s rotation period), a magneto-rotational explosion may arise within a few hundred milliseconds of core bounce, with a potential to produce an axisymmetric and highly energetic explosion (LeBlanc & Wilson 1970; Bisnovatyi-Kogan et al. 1976; Symbalisty 1984; Akiyama et al. 2003; Moiseenko et al. 2006; Uzdensky & MacFadyen 2007; Burrows et al. 2007a; Dessart et al. 2008b). A variety of potential mechanisms thus exists to power a wide range of core-collapse SN explosions, with energy perhaps as

* E-mail: Luc.Dessart@oamp.fr

low as 0.01 B and as high as 10 B, and with a morphology departing quite naturally from spherical symmetry. However, it is currently difficult to go beyond such general statements, by quantitatively characterising the specific properties of the progenitor stars associated with the core-collapse SNe we see and by assessing how they exploded.

An important question is to determine if there is an upper-limit to the main-sequence star mass for a successful core-collapse SN explosion. This is relevant for determining the chemical yields and the properties/identity of the compact object produced by the event, but also for the understanding of the mechanism of explosion and its dependency on, e.g., stellar structure. Currently, identification of the SN progenitor on pre-explosion images has been possible for a handful of cases, and primarily for the Type II-Plateau (II-P) SNe, confirming their progenitors are red-supergiant (RSG) stars (see, e.g., Van Dyk et al. 2003; Smartt et al. 2004; Maund et al. 2005; Li et al. 2006; Mattila et al. 2008). Surprisingly, such observations also suggest that these progenitors have a main-sequence mass in the range $\sim 8.5\text{--}16.5 M_{\odot}$ (see Smartt 2009 and references therein), which is at the lower end of the range expected from stellar evolutionary calculations. On the other hand, radiation-hydrodynamics simulations of SNe II-P light curves and their photospheric-velocity evolution generally support larger masses, at odds with observational inferences (see, e.g., Utrobin & Chugai 2009). An issue here is our ability to distinguish between inferences on the final mass (that at core collapse), and the initial mass (that on the main sequence).

Observationally, and until neutrino and gravitational-wave detectors obtain their novel signatures associated with a core-collapse SN, photons represent the main source of information for inferring the properties of the ejecta and their progenitors. Because of its relative simplicity, bolometric light-curve modelling has been the main tool. In the context of hydrogen-rich core-collapse SNe, the emergent radiation is primarily conditioned by the properties of the progenitor star, i.e. its final mass and in particular the mass/size of its hydrogen-envelope, and the properties of the explosion, i.e. the energetics and the mass of nucleosynthesized ^{56}Ni (Falk & Arnett 1977; Popov 1993; Nadyozhin 2003; Baklanov et al. 2005; Utrobin 2007; Kasen & Woosley 2009; Dessart et al. 2010). These observables appear, however, quite degenerate (see, e.g., Hamuy 2003; Bersten & Hamuy 2009) and do not seem to manifest much dependency on the properties of the progenitor helium core. Their interpretation is complicated by multiple factors associated with the explosion mechanism, as discussed above, but also by the uncertainties in the pre-SN star mass, which is affected by mass loss.

Stellar-wind mass loss, in particular during the RSG phase, peels off the hydrogen envelope of a $10\text{--}30 M_{\odot}$ progenitor massive star and leaves it with a much reduced mass (this reduction depends on stellar mass) by the time of core collapse. The mean RSG mass-loss-rate value appears to be on the order of $10^{-5}\text{--}10^{-6} M_{\odot} \text{ yr}^{-1}$ (de Jager et al. 1988), but large uncertainties exist owing to the incomplete knowledge of the mass loss mechanism (see, e.g., Josselin & Plez 2007). The cumulative loss of mass is conditioned by the duration of that RSG phase, which can be lengthened by stellar rotation (Meynet et al. 2006). These objects may also go through “super-wind” phases with mass-loss rates as high as $\sim 10^{-4} M_{\odot} \text{ yr}^{-1}$, in particular in the ultimate stages of evolution (Heger et al. 1997; Yoon & Cantiello 2010). The presence of massive nebulae around such RSG stars suggests that dramatic mass-loss events can take place (Smith et al. 2009). In some, they may even be triggered by nuclear flashes at the surface of the degenerate core (Weaver & Woosley 1979), with dramatic conse-

quences for their loosely-bound massive hydrogen-rich envelopes (Dessart et al. 2010). When extended to include binary-star evolution channel, these issues become even more complicated. The likely important role of binary-star evolution to the making of SN progenitors remains to be thoroughly explored (in the context of SNe associated with a γ -ray burst, see, e.g., Cantiello et al. 2007). Overall, these complications make the final mass and radius of the pre-SN II-P progenitor uncertain.

In contrast, a key property of single-massive stars is their increasing helium-core mass with main-sequence mass (and rotation). When considering SN II progenitors, the helium-core mass is not affected by mass loss since a residual hydrogen envelope is still present. In Type Ib/c SN progenitors, mass loss is thought to have not only peeled away the hydrogen envelope, but also the helium core itself, braking the unique association between progenitor mass and helium-core mass.¹ Hence, in SNe II, while there may be doubt on the mass of hydrogen endowed by a given massive star at collapse (and more generally the final mass), the mass of the helium core is very strictly set by stellar structure/evolution and is independent of the mass-loss history of the star. In the range between 11 and $30 M_{\odot}$, this helium-core mass grows enormously, from around $1.5\text{--}2 M_{\odot}$ up to $8\text{--}10 M_{\odot}$ (Woosley & Weaver 1995; Woosley et al. 2002; Arnett 1991). Hence, ignoring for now stellar rotation, the main-sequence mass ties directly with the helium-core mass, and could be inferred provided the latter is somehow constrained from the SN light.

The amount of information that can be extracted from SN II-P light curves alone is limited. This stems from the fact that the *plateau phase* that is generally the focus of attention provides restricted information, primarily on the shocked hydrogen-envelope, whose pre-shocked properties are made uncertain because of mass loss. It provides no unambiguous information on chemical yields, no information on the distribution of elements in velocity space or on the properties of the progenitor helium core, no direct evidence for mixing etc. In contrast, having recourse to both SN spectra and light-curves, together with sophisticated radiative-transfer and radiation-hydrodynamics tools to model them, can alleviate these shortcomings. This modelling approach can apply even for distant Type II-P SNe and is thus advantageous over the direct identification of progenitors on pre-explosion images, which only works for nearby objects (perhaps up to ~ 20 Mpc).

For this study, we generated a wide range of SN II-P explosions, using the one-dimensional grey radiation-hydrodynamics code *V1D* (Livne 1993; Dessart et al. 2010), and starting our simulations from the pre-SN models for non-rotating and rotating massive stars computed *at solar metallicity* by Woosley et al. (2002, hereafter, WHW02) and Heger et al. (2000, hereafter, HLW00), respectively. Leaving to a forthcoming paper the full presentation of non-local thermodynamic equilibrium (non-LTE) synthetic spectra and light curves (Dessart et al, in preparation), we focus the discussion here on the properties of such SN II-P ejecta, in particular the chemical distribution in velocity space. This has already been discussed in the past, but usually merely “in passing”, by studies of chemical yields of core-collapse SN explosions in the modern or early Universe (Woosley & Weaver 1995; Tominaga et al. 2007; Heger & Woosley 2008; Tominaga 2009; Joggerst et al. 2010),

¹ Binary-star evolution, with mass transfer and the possible evolution through a common envelope phase, is a further complication (Taam & Ricker 2006). However, the final product might not die as a RSG and not give rise to a SN II-P.

Table 1. Summary of the properties for a representative sample of pre-SN models employed in this study. From the upper part to the lower part of the table, we show properties for non-rotating (“s” series; WHW02) and rotating (“E” series; HLW00) pre-SN models. For each, we give the initial mass M_i (i.e. the main-sequence mass), the final mass M_f (i.e. the mass at core collapse), the Lagrangian mass delimiting important shells (outer edge of the core M_{core} ; outer edge of the oxygen shell $M_{\text{e,O}}$; outer edge of the helium shell $M_{\text{e,He}}$; inner edge of the hydrogen shell $M_{\text{i,H}}$), the mass M (H env.) and the size ΔR (H env.) of the hydrogen-rich envelope, the surface radius R_* , the gravitational and binding energies (E_{grav} and E_{binding}) of the progenitor envelope outside of M_{core} . [See text for discussion]

Pre-SN Model	M_i [M_\odot]	M_f [M_\odot]	M_{core} [M_\odot]	$M_{\text{e,O}}$ [M_\odot]	$M_{\text{e,He}}$ [M_\odot]	$M_{\text{i,H}}$ [M_\odot]	M (H env.) [M_\odot]	ΔR (H env.) [10^{13} cm]	R_* [10^{13} cm]	E_{grav} [B]	E_{binding} [B]
s11	11.0	10.61	1.37	1.69	1.75	2.78	7.83	4.06	4.086	0.342	0.135
s15	15.0	12.64	1.62	2.61	3.00	4.15	8.49	5.86	5.867	0.995	0.392
s20	20.0	14.73	1.46	4.25	4.95	6.14	8.59	7.81	7.816	1.411	0.399
s25	25.0	12.53	1.92	5.71	7.15	8.40	4.13	10.06	10.066	3.310	0.858
s30	30.0	12.24	2.04	7.72	9.18	10.02	2.22	8.51	8.516	2.984	0.744
E10	10.0	9.23	1.48	1.72	1.82	2.89	6.34	3.82	3.842	0.354	0.170
E12	12.0	10.35	1.50	2.31	3.49	3.72	6.63	5.26	5.271	0.637	0.213
E15	15.0	10.86	1.62	3.39	4.94	5.19	5.68	7.51	7.515	1.318	0.402
E20	20.0	11.01	1.84	4.38	7.75	7.96	3.05	15.63	15.643	2.465	0.718

chemical mixing by Rayleigh-Taylor instabilities in the first few hours of the life of the SN (Herant & Woosley 1994; Mueller et al. 1991; Kifonidis et al. 2000, 2003, 2006; Hammer et al. 2009), or in the context of the remnant mass (see, e.g. Zhang et al. 2008). Here, we emphasise that strong constraints can be placed on the main-sequence mass of a SN II-P progenitor from the ejection-speed of core-embedded oxygen-rich material and the expansion-rate of the hydrogen-rich progenitor envelope.

This paper is structured as follows. In §2, we summarise the properties of the progenitor models used in this study, as well as the numerical setup for our one-dimensional grey radiation-hydrodynamics simulations using the code V1D (Livne 1993; Dessart et al. 2010). We then present in §3 the ejecta kinematics we obtain for a variety of progenitor stars and explosion parameters, and discuss how such properties can be used to constrain the progenitor main-sequence mass. Separately, in an appendix, we present other results obtained from this grid of models. In §4, we conclude and confront our results to observations. In particular, we discuss how one can attempt to spectroscopically constrain a SN II-P progenitor main-sequence mass from the observation of nebular-phase OI 6303-6363Å and photospheric-phase optical spectra.

2 PROGENITOR MODELS AND NUMERICAL SETUP

2.1 Progenitor models

Our radiation-hydrodynamics study employs as starting conditions two different sets of stellar evolutionary calculations for massive stars at solar metallicity and with allowance for mass loss. We use both the non-rotating pre-SN models of WHW02, with main-sequence mass in the range 11–30 M_\odot (model prefix “s”), and the rotating pre-SN models of HLW00, with main-sequence mass in the range 10–20 M_\odot (model prefix “E”; the initial equatorial velocity is 200 km s^{−1}). We refer the reader to the corresponding references for details on these evolutionary calculations. In each case, the evolution is computed until the onset of collapse of the degenerate core. This choice of mass range is motivated by our desire to select only those progenitors that have retained a hydrogen envelope massive enough to produce a SN II-P when exploded. Hence, for all of these pre-SN models, mass loss has not had any erosive ef-

fect on the helium-core, whose mass is thus an increasing function of main-sequence mass.

In Table 1, we give a summary of the properties for a representative sample of the (non-rotating) WHW02 pre-SN models, i.e. models s11, s15, s20, s25, and s30, as well as those for our set of (rotating) HLW00 pre-SN models (E10, E12, E15, and E20). We give the approximate edge location of the oxygen/helium/hydrogen shells, adopting the depth where the mean molecular weight drops outward below 16.5/4.5/2.0, respectively. Note in particular that, for non-rotating models in the mass range 11–30 M_\odot , the helium core mass grows from 1.75 up to 9.18 M_\odot , while the final star mass at collapse varies little and is in the range 10.61–14.73 M_\odot . Hence, in these non-rotating models, the helium-core mass represents from 16% up to 75% of the total star mass at the onset of collapse (the relative fraction of the star that represents the hydrogen-rich envelope decreases correspondingly). We illustrate the chemical stratification of these pre-SN models in the left panel of Fig. 1, selecting oxygen and hydrogen for better visibility. For more massive main-sequence objects, oxygen is globally more abundant and is present closer (in mass coordinate) to the surface.

In the lower part of Table 1, we summarise the properties of the rotating pre-SN models of HLW00, showing the envelope chemical stratification in the right panel of Fig. 1. Rotation produces bigger helium cores for a given star mass, so that models E15 and s20 have similar helium-core masses despite having 15 and 20 M_\odot main-sequence masses, respectively. Furthermore, because of enhanced mixing and mass loss, the maximum mass for a rotating star to produce a SN II-P is lowered. Here, the HLW00 models suggest that stars initially more massive than ~20 M_\odot will not retain any hydrogen by the time of collapse and thus cannot lead to a SN II event.

A generic feature of all these hydrogen-rich massive stars is that their hydrogen-rich envelope is always very loosely bound (Dessart et al. 2010). It is very extended and represents typically 99% of the size of the star, so that the helium core is contained in the inner few percent of the stellar radius. The gravitational energy scaling with the square of the mass (but only with the inverse of the radius), the helium core becomes increasingly more bound in higher-mass progenitors. With the increase of the helium core mass with main-sequence mass, the mean envelope binding energy of the pre-SN progenitor star increases with main-sequence mass (see Table 1). Ultimately, this conditions the successful ejection of helium-

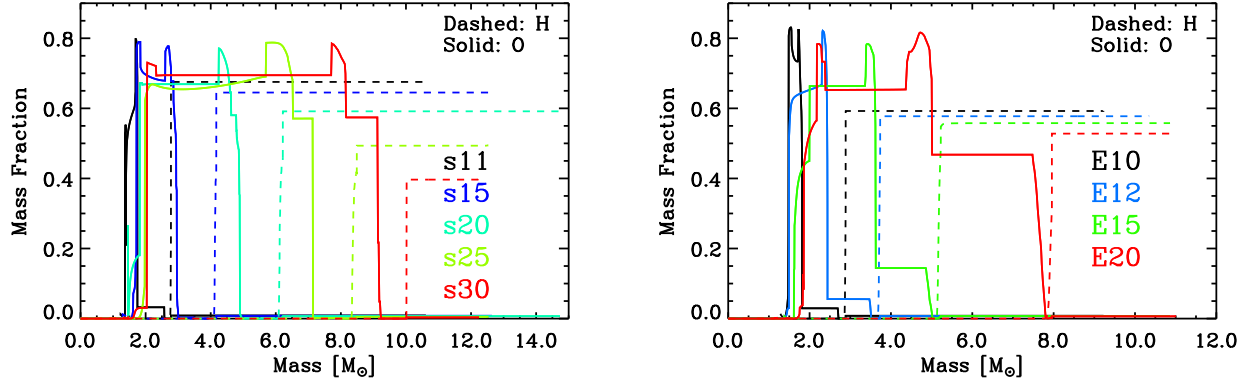


Figure 1. Illustration of the distribution of hydrogen (dashed) and oxygen (solid) versus Lagrangian mass in the envelope of a few non-rotating (left; “s” series from WHW02) and rotating (right; “E” series from HLW00) pre-SN models. A colour coding is used to differentiate models of differing main-sequence mass (given by the number XX in sXX or EXX; see Table 1). Notice the growing mass of the oxygen-rich shell with increasing main-sequence mass, and for a given main-sequence mass when rotation is included. [See text for discussion].

core material and the magnitude of fallback (Woosley & Weaver 1995; Zhang et al. 2008).

2.2 Radiation-hydrodynamics simulations with `V1D`

Starting with the pre-SN progenitor models described above, we then employ the one-dimensional grey (i.e. one-group) flux-limited-diffusion radiation-hydrodynamics code `V1D` to simulate a core-collapse SN explosion. A description of this version of the code is given in Dessart et al. (2010) and will not be repeated here since the numerical approach is basically the same, apart from the energy deposition procedure. In the past, our approach was to simply deposit internal energy at a specified rate and up to a given amount at the base of the grid, chosen at some mass cut. For this study, we find it more practical to generate the explosion by driving a piston at the grid base. This is the standard, albeit artificial, way of generating a SN ejecta when modeling SN light curves and asymptotic ejecta properties. Excising the core region alleviates the Courant-time limitation and permits the simulation of one model out to one year within 1–2 days on a single processor. Following the collapse, bounce, and post-bounce phases of the entire object all the way to one year would instead be a computational challenge, also compromised by the incomplete knowledge of the explosion mechanism.

To set the piston properties (mass cut M_{piston} and speed V_{piston}), we guide ourselves with results from multi-dimensional (neutrino) radiation-hydrodynamics simulations of core-collapse SN explosions. Whatever the explosion mechanism (see introduction for a concise summary), recent simulations suggest the explosion appears with a delay of a few hundred milliseconds after core bounce. This delay is necessary to increase the neutrino-energy deposition in the gain region for neutrino-driven explosions (see, e.g., Marek & Janka 2009), or to achieve the necessary magnetic-field amplification in magneto-rotational explosions of fast-rotating progenitor stars (see, e.g., Burrows et al. 2007a). Owing to the different iron-core structure of massive stars of various main-sequence mass, this will correspond to different mass cuts at the onset of explosion. In practice, we determine the piston mass cut by performing core-collapse simulations for each of our WHW02/HLW00 pre-SN model using the code `GR1D` (O’Connor & Ott 2010). The simulations were done using the stiff nuclear Equation of State they

provide, general-relativistic gravity, and a leakage scheme (combined with a parameterisation of the electron fraction with mass density) for the treatment of deleptonisation. In all such simulations, the PNS mass rapidly grows after core bounce due to the huge initial accretion rates, but this mass evolves slowly past a few hundred milliseconds post-bounce time. Furthermore, at such times, the enclosed mass between the PNS surface and a radius of 1000–2000 km is a small fraction of the PNS mass. Hence, we assigned to M_{piston} the value obtained in our GR1D simulations for the accumulated baryonic mass enclosed in the inner 500 km at a post-bounce time of 500 ms (fourth-column entry in Tables 2–6). Our resulting choice for M_{piston} agrees to within 0.1–0.2 M_{\odot} with the values used by Woosley & Weaver (1995) or more recently by Zhang et al. (2008). We find that variations of a few 0.1 M_{\odot} in the choice of M_{piston} value have no effect on the results for the ejecta kinematics (provided the energy deposited is adjusted to account for the modulation in the binding energy of the material outside of M_{piston}).

Once initiated, the explosion does not occur promptly - the energy is deposited over a finite time. In their simulation of a 15 M_{\odot} star, Marek & Janka (2009) find promising signs for a successful neutrino-driven explosion starting at ~ 500 ms, but a few hundred milliseconds or even a full second may be needed to reach an energy of 1 B (there is structure in their curves of, e.g. Fig. 9, which makes it difficult to extrapolate in confidence). In the context of magneto-rotational core-collapse SN explosions, Burrows et al. (2007a) and Dessart et al. (2008b) find their simulations reach ~ 1 B about 300 ms after the shock is launched, while a full second will be needed to deliver the additional energy to unbind the envelope and boost it to hypernova energies they seem capable of reaching. In practice, and given all these uncertainties, we simply adopt a constant piston speed V_{piston} , with values of 10000 and 20000 km s^{-1} . As illustrated in the left panel of Fig. 2, this choice covers the extremes from a sudden (energy deposition over ~ 100 ms) to a slow-developing explosion (energy deposition over ~ 1 s). Once the piston has delivered the energy aimed for, it is stopped.

The approach of Woosley & Weaver (1995) is similar but somewhat more complicated. They first position the piston at some mass cut M_{cut} , let it dynamically collapse until a radius of $R_{\text{min}} = 500$ km where it is suddenly set in outward motion with an ini-

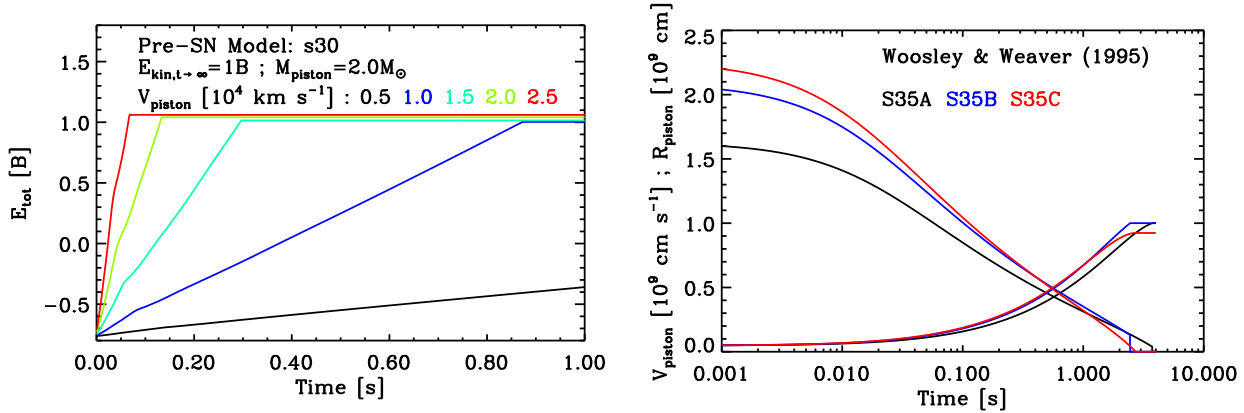


Figure 2. *Left:* Illustration of the evolution of the total ejecta energy in our v1D simulations based on the pre-SN model s30 characterised by $E_{\text{kin}}=1\text{B}$ and piston speeds of 5000 (black), 10000 (blue), 15000 (turquoise), 20000 (green), and 25000 km s^{-1} (red). For the former model, it requires about 5 s to reach the desired ejecta kinetic energy, which is much too long, while for the latter, it takes no more than 60 ms, which is much too short. A guess compatible with current state-of-the-art simulations of core-collapse SN explosions would be on the order of 10000 km s^{-1} . *Right:* Illustration of the piston velocity (downward-pointing curve) and radius (upward-pointing curve) for the simulations S35A, S35B, and S35C of Woosley & Weaver (1995). [See text for discussion].

tial velocity V_0 . At subsequent times, the piston trajectory $R(t)$ is given by $dR/dt = (\alpha GM_{\text{cut}}(1/R - 1/R_{\text{min}}) + V_0^2)^{1/2}$, until it reaches 10000 km where it is stopped (α is some adjustable parameter). With such a trajectory, the bulk of the energy is deposited at early times, when the piston speed is maximum. We show in the right panel of Fig. 2 the resulting piston radii and velocities for their simulations S35A ($V_0 = 16000 \text{ km s}^{-1}$, $\alpha = 0.50$, and $E_{K\infty} = 1.23\text{B}$), S35B ($V_0 = 20400 \text{ km s}^{-1}$, $\alpha = 0.81$, and $E_{K\infty} = 1.88\text{B}$), and S35C ($V_0 = 22000 \text{ km s}^{-1}$, $\alpha = 0.95$, and $E_{K\infty} = 2.22\text{B}$), where $E_{K\infty}$ is the asymptotic ejecta kinetic energy. In these three cases, they obtain remnant masses of 7.38, 3.86, and $2.03 M_{\odot}$, respectively. The last value corresponds to their adopted choice of M_{cut} , which thus suggests no fallback for simulation S35C. The properties of the compact remnant are visibly affected by the explosion energy and the choice of piston speed. In their study, Woosley & Weaver (1995) adopt reference piston speeds V_0 in the range 12000 up to 37000 km s^{-1} . In this work, we find that our results for the remnant mass (see appendix and Tables 2–5) are comparable to those of Woosley & Weaver (1995) for a piston speed of 20000 km s^{-1} , which corresponds to a very short energy-deposition timescale of $\sim 100 \text{ ms}$ (left panel of Fig. 2). Since it seems that the shock revival/powering takes place on a longer timescale, their choice of piston speeds may be somewhat overestimated (and consequently their remnant masses underestimated).

As the mass of the core increases from low-mass to high-mass massive stars, a growing fraction of the helium core eventually falls back. This fallback material remains dense and hot and limits the progress of the simulation to late times. Hence, all our simulations are halted at 20000 s after the piston trigger. Any material in the inner ejecta moving with a velocity smaller than the local escape speed is trimmed and the simulation is restarted. This rough treatment likely affects the accuracy of the remnant mass, although our results agree closely with those of Woosley & Weaver (1995) when similar parameters are used. In contrast, for a given energy deposition, the adopted piston trajectory does not alter sizeably the key ejecta kinematics, which are the focus of the present study.

We perform no mixing/smoothing on the progenitor structure, neither prior to nor after the explosion is launched, and thus do not

test the potential (and expected) impact asymmetric explosions or Rayleigh-Taylor instabilities would have on observables.

Since the bulk of our discussion is on the ejecta properties, rather than on the emergent radiation, we do not treat energy deposition from unstable isotopes like ^{56}Ni . When included, the associated decay energy is known to lengthen the high-brightness part of the light curve. This will be important for the computation of detailed non-LTE time-dependent light curves and spectra using the approach of Dessart & Hillier (2010), which is left to a forthcoming paper. Hence, all plateau durations given in Tables 2–6 represent a lower limit.

In the next section, we present results from our simulations. The nomenclature for our models is such that our simulation called s11e10m147v20 corresponds to one based on the WHW02 pre-SN model s11, exploded to yield a 1 B ejecta kinetic energy at infinity (e10), adopting a piston mass cut at $1.47 M_{\odot}$ (m147) and a piston speed of 20000 km s^{-1} (v20). In practice, we have run simulations for WHW02 pre-SN models s11 up to s30 at every $1 M_{\odot}$ increment in main-sequence mass (i.e. s11, s12, s13 etc.), but run only simulations for the E10, E12, E15, and E20 rotating pre-SN models of HLW00. Note also that for low-energy explosions, the fallback material prevents an easy guess of the asymptotic ejecta kinetic energy (only a fraction of the mass placed on the grid will be kept after trimming the fallback material, hence changing the total energy on the grid with time). For “e01” models (energy deposition to yield a 0.1 B ejecta kinetic energy), the simulations ended up asymptotically with an energy as high as $\sim 0.2\text{B}$, while for more energetic explosions, the two energies agreed within a few percent. This and numerous other results from our simulations are given in Tables 2–6.

3 RESULTS

In this section, we present the results from the radiation-hydrodynamics simulations with v1D and based on the pre-SN progenitor models of WHW02 (prefix “s”; no rotation) and HLW00 (prefix “E”; with rotation) - see Table 1 for details. A full log of our simulation results is presented in Tables 2–6, with additional

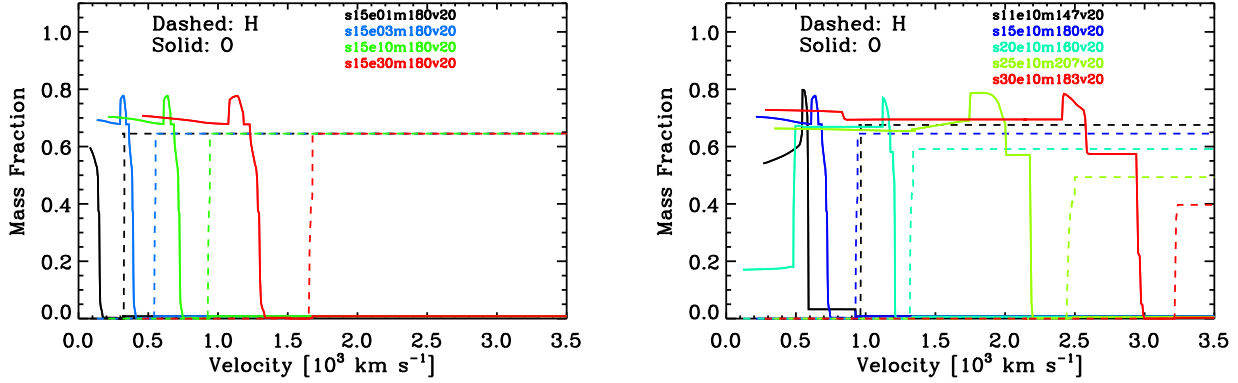


Figure 3. *Left:* Distribution of hydrogen (dashed line) and oxygen (solid line) with respect to ejecta velocity for simulations s15e01m180v20 (black), s15e03m180v20 (blue), s15e10m180v20 (green), and s15e30m180v20 (red), all based on the *same pre-SN model* s15. The time is 70 days after explosion, thus when homology is well established. Notice the systematic location of oxygen at larger velocities for increasing asymptotic ejecta kinetic energy. *Right:* Same as left, but now showing the results for simulations s11e10m147v20 (black), s15e10m180v20 (blue), s20e10m160v20 (turquoise), s25e10m207v20 (green), and s30e10m183v20 (red), having the *same ejecta kinetic energy* of 1 B but differing in pre-SN model. The range of velocities we obtain for the outer edge of the oxygen-rich shell is now much larger. [See text for discussion]

information given in the appendix. Our exploration is over pre-SN models that differ in their main-sequence mass (we adopt the mass range 11–30 M_{\odot} for non-rotating models and 10–20 M_{\odot} for rotating models) and piston trajectories that yield asymptotic ejecta kinetic energies of 0.1, 0.3, 1.0, and 3.0 B.

Our simulations based on such pre-SN models yield successful explosions that would be characterised as a II-P event (the progenitor stars are RSGs with a massive hydrogen-rich envelope). The general evolution after the piston trigger of the resulting shock-heated envelopes is the following. After a delay corresponding to the shock-crossing time through the envelope (which we denote t_{SBO}), the ejecta expand and accelerate for a few days until reaching a coasting phase in which all mass parcels move at a constant velocity. Expansion causes dilution and a decrease of the ejecta optical depth as the inverse square of the time, reduced further by the recombination of ions to their neutral state. While the photosphere (defined as the location where the inward-integrated continuum optical depth equals 2/3) moves initially outward in radius, within about 30–50 d of shock-breakout it stabilises at a radius of $\sim 10^{15}$ cm and gives a plateau to the SN light curve (Dessart et al. 2008a). This “photospheric” phase ends when the ejecta become optically-thin in the continuum. While this scenario holds qualitatively in all the simulations we performed for this work, differences in the pre-SN models and/or the adopted explosion parameters can lead to significant quantitative differences. A number of studies have focused on the resulting properties of the emergent light, such as recently Kasen & Woosley (2009), and are thus not presented in detail here, although we give a comprehensive summary of our results in the Appendix and Tables 2–6. However, since this has not been discussed in detail elsewhere, we focus here on the properties of the SN ejecta kinematics and chemical stratification. Ultimately, our goal is to identify spectroscopic observables that can complement the restricted information provided by the light curve in order to better constrain the properties of the progenitor star and the explosion physics.

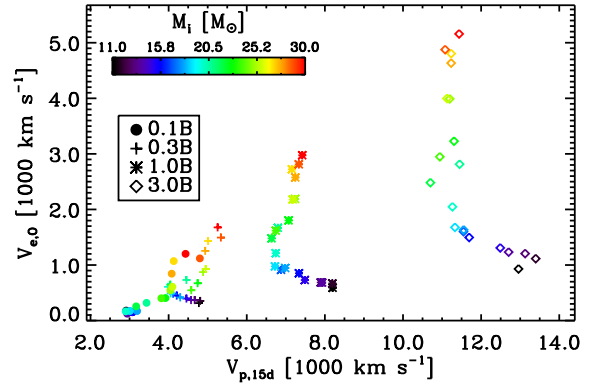


Figure 4. Distribution of the velocity at the outer edge of the oxygen-rich shell $V_{e,O}$ as a function of the ejecta photospheric velocity at 15 d after shock-breakout $V_{p,15d}$ for our 1D simulations adopting a piston speed of 20000 km s^{-1} , and set up to yield an asymptotic ejecta kinetic energy of 0.1 B (dots), 0.3 B (pluses), 1 B (asterisks), and 3 B (diamonds). We employ a colour-coding to give the main-sequence mass for each model. With this nomenclature, the model s11e01m147v20 appears as a black dot, and the model s30e30m183v20 as a red diamond. Comprehensive results from our simulations are given in Tables 2–5.

3.1 Results based on non-rotating pre-SN models

For a given progenitor mass, increasing the energy deposited by the piston yields an ejecta with a higher kinetic energy at infinity and a larger velocity in each mass shell. With ejecta kinetic energy of ~ 0.1 , 0.3, 1.0, and 3.0 B, simulations s15e01m80v20, s15e03m80v20, s15e10m80v20, and s15e30m80v20 show a maximum velocity of the outer-edge of the oxygen shell $V_{e,O}$ at 155, 396, 730, 1308 km s^{-1} , hence encompassing about a factor of ten in this set corresponding to the pre-SN model s15 (left panel of Fig. 3). The velocity at the inner edge of the hydrogen-rich envelope $V_{i,H}$, which is located just outside of the oxygen-rich shell in the pre-SN progenitor envelope (the two are separated by a narrow helium-rich shell), is generally a few 100 km s^{-1}

larger and thus does not require a specific discussion. But if we fix the energy deposition to yield an ejecta kinetic energy of 1 B and now vary the main-sequence mass of the pre-SN model, from 11 to $30 M_{\odot}$, the range of values for $V_{e,O}$ is considerably enhanced. In the right panel of Fig. 3, we show such results for our simulations s11e10m147v20, s15e10m180v20, s20e10m160v20, s25e10m207v20, and s30e10m183v20, which give values of $V_{e,O}$ now stretching from 590 to 2975 km s^{-1} . The larger size of the helium-core for larger main-sequence mass stars produce SN ejecta that eject core-embedded oxygen-rich material at a larger velocity for a *given* ejecta kinetic energy. This stems naturally from the fact that in larger mass progenitors, the bigger helium core represents a larger fraction of the total mass, i.e. the outer oxygen-rich shell is located closer to the progenitor surface. We stress here that this result depends primarily on the *main-sequence* mass, since it determines the mass of the helium core. This is somewhat paradoxical because the SN radiation is generally interpreted in terms of the properties of the star at the time of collapse. In SNe II, mass loss does not alter the mass of the helium core, and the connection to the main-sequence mass of the progenitor can therefore be made. The final mass at collapse does, however, enter the problem as it sets the magnitude of the mass-weighted mean ejecta velocity. However, our set of pre-SN models shows a very narrow range of values for the final mass so that the trend observed here is controlled primarily by the large variation in $M_{e,O}/M_f$ rather than the modest variation in M_f .²

These results suggest that in SN II-P ejecta, both explosion energy and progenitor main-sequence mass correlate with the asymptotic value of $V_{e,O}$. The explosion energy can be determined independently, as it affects the mean velocity of the ejecta, which can be inferred through an estimate of the photospheric velocity at some given time. Here, we use the ejecta photospheric velocity at 15 d after shock breakout, $V_{p,15d}$. This measurement can be done using spectroscopic observations and fitting hydrogen Balmer lines by means of radiative-transfer simulations (Dessart & Hillier 2005b). Alternatively, one can use the photospheric velocity at 50 d after explosion ($V_{p,50d}$), inferred through a measurement of the Doppler-velocity corresponding to maximum P-Cygni-profile absorption in FeII 5169 Å (Dessart & Hillier 2005a; Kasen & Woosley 2009; Dessart & Hillier 2010). In Fig. 4, we now show the resulting distribution of values of $V_{e,O}$ versus $V_{p,15d}$ for a large set of simulations based on the non-rotating pre-SN models of WHW02. A colour-coding is used to differentiate the initial (main-sequence) mass of each model, while symbols are used to differentiate the asymptotic kinetic energy aimed for (dots: 0.1 B; pluses: 0.3 B; asterisks: 1.0 B; diamonds: 3.0 B). Models of distinct ejecta-kinetic energy are now well separated, provided this energy is ~ 0.3 B or larger. High-energy explosions of 3.0 B are characterised by $V_{p,15d} \gtrsim 10000 \text{ km s}^{-1}$, with values of $V_{e,O}$ ranging from $\sim 1000 \text{ km s}^{-1}$ up to 5000 km s^{-1} . For the more standard explosion energy of 1.0 B, $V_{p,15d} \sim 7000 \text{ km s}^{-1}$, and values of $V_{e,O}$ range from 500 km s^{-1} up to a lower maximum of 3000 km s^{-1} . For yet lower explosion energies, values of $V_{e,O}$ and $V_{p,15d}$ continue to decrease and start to overlap.³ However,

² The set of pre-SN stellar-evolution models from WHW02 and HLW00 were computed with specific prescriptions for the treatment of mass loss etc. The trends we identify hence apply to these pre-SN models and would be altered if, for example, we were to take Population III star models.

³ As the energy is lowered, the distributions become more compact and a unique association of $V_{e,O}$ and $V_{p,15d}$ is difficult. This results in part from a problem in our simulations of low-energy explosions for higher mass

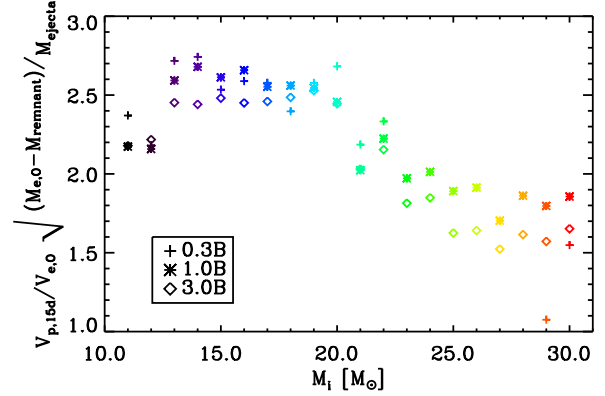


Figure 5. Illustration of the variation of the quantity $\frac{V_{p,15d}}{V_{e,O}} \sqrt{\frac{M_{e,O} - M_{\text{remnant}}}{M_{\text{ejecta}}}}$ versus initial mass M_i for our v1D simulations based on the non-rotating pre-SN models of WHW02 and exploded to yield an asymptotic ejecta kinetic energy of 0.3 (pluses), 1.0 (asterisks), or 3.0 B (diamonds; the symbol and colour assignment is the same as that used in Fig. 4). Note that we exclude from this figure the simulations that use an explosion energy of 0.1 B since in this situation, the fallback magnitude is huge and no core-embedded oxygen-rich material is ejected ($M_{e,O} < M_{\text{remnant}}$). This issue also applies to a few simulations with an explosion energy of 0.3 B for pre-SN models with a main-sequence mass between 23 and $28 M_{\odot}$. [See text for discussion].

for explosion energies of 0.3 B or less, values of $V_{e,O}$ are systematically below 2000 km s^{-1} , while values of $V_{p,15d}$ never exceed 6000 km s^{-1} . Note that the kink in the distribution of data-points in Fig. 4 for initial masses of $\sim 20 M_{\odot}$ corresponds to the pre-SN models in our sample that have the largest mass at the time of collapse, hence the lowest mean-ejecta velocity for a given explosion energy (they have the lowest kinetic energy per unit mass).

The apparent scatter of data-points shown in Fig. 4, both with explosion energy and pre-SN model, can be reduced by inspecting dependent variables. In our set of simulations, we recover the scaling of the ejecta velocity with the square-root of energy over mass. For example, we find that the ratio of $V_{e,O}$ and $\sqrt{e_{\text{kt}}/(M_{e,O} - M_{\text{remnant}})}$ is independent of the ejecta kinetic energy e_{kt} (note, however, that this ratio varies significantly with pre-SN model, reflecting variations in $M_{e,O}/M_f$). Here, $V_{e,O}$ is a representative ejection velocity for the core-embedded oxygen-rich material, whose mass scales with $M_{e,O} - M_{\text{remnant}}$. The above scaling holds provided the fallback is never too large to yield $M_{e,O} < M_{\text{remnant}}$, a circumstance that characterises under-energetic explosions. We also find that $V_{p,15d}$ over $\sqrt{e_{\text{kt}}/M_{\text{ejecta}}}$ is independent of explosion energy. The quantity $X = \frac{V_{p,15d}}{V_{e,O}} \sqrt{\frac{M_{e,O} - M_{\text{remnant}}}{M_{\text{ejecta}}}}$, is thus independent of energy. As shown in Fig. 5 (our v1D simulations with explosion energy of 0.1 B experience complete fallback of the core-embedded oxygen-rich material and are thus not plotted in this figure), simulations for a given pre-SN model but different explosion energies show X values that are generally within $\sim 10\%$ of each other.

stars, which are all characterised by a large fallback mass. In these simulations, the fallback mass takes away binding energy and leads to overestimated energies for the ejected material. In such under-energetic explosions, hardly any core-embedded oxygen-rich material is ejected, making the discussion of $V_{e,O}$ somewhat irrelevant in this situation.

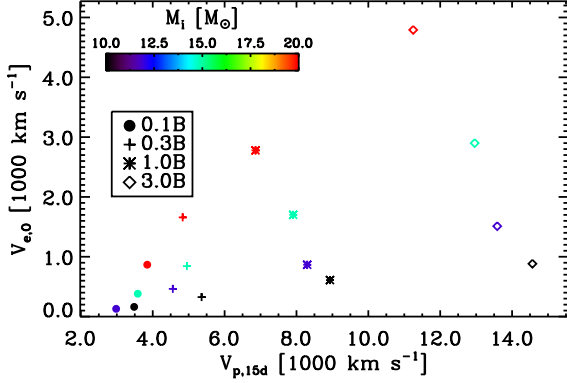


Figure 6. Same as Fig. 4, but now for our simulations based on a set of rotating pre-SN models. Comprehensive results from our simulations are given in Table 6. [See text for discussion].

The uniformity of values of $V_{p,15d}$ for a given explosion energy but a range of pre-SN models (Fig. 4) suggests it is a rough but easy diagnostic of the explosion energy characterising a SN II-P. The large range in progenitor main-sequence mass for our set of pre-SN models also suggests that it should not be dramatically altered by uncertainties in stellar evolution and thus represents a valuable guide (unless the mass-loss rate prescriptions used in the pre-SN stellar evolutionary calculations are way off). Having estimated the explosion energy through a measurement of $V_{p,15d}$, the value of $V_{e,O}$ can place tight constraints on the progenitor main-sequence mass. Our results suggest that main-sequence stars less massive than $\sim 20 M_{\odot}$ tend to produce SN II-P ejecta with values of $V_{e,O}$ smaller than 500, 1000, and 2000 km s^{-1} , for explosion energies of 0.3, 1.0, and 3.0 B, respectively. For any explosion energy in the range 0.1 to 3.0 B, simulations based on the s11 pre-SN model show values of $V_{e,O}$ that are systematically below 1000 km s^{-1} while those based on the s30 pre-SN model show values always in excess of 1000 km s^{-1} no matter what the explosion energy is. The maximum speed of the oxygen-rich shell sets therefore a very strong constraint on the progenitor mass of SNe II-P, distinguishing between a low-mass or a high-mass massive star as the progenitor.

The above simulations employ a piston speed of 20000 km s^{-1} . As shown in Tables 2–6, employing a piston speed of 10000 km s^{-1} for the same set of pre-SN models does not in general alter by more than $\sim 10\%$ the values previously found (one exception is when the lowering of the piston speed leads to fallback of the entire helium core, as happens for model E20e10m200v10 compared to model E20e10m200v20). This suggests that, in the present (1D) context, the ejecta kinematics are very sensitive to the explosion energy, but not to the details of the explosion mechanism nor the way we numerically explode these pre-SN stars (e.g. the exact value of M_{piston}).⁴

3.2 Results based on rotating pre-SN models

As emphasised above, the helium-core mass is a growing function of main-sequence mass. However, stellar rotation breaks this simple correlation, as it tends to increase the helium-core mass

for a given main-sequence mass. We then anticipate that the values of $V_{e,O}$ presented above for non-rotating progenitors place an *upper-limit* on the main-sequence mass of a given SN progenitor. We thus performed another set of simulations, using the same procedure as above for the non-rotating models, but now employing the rotating pre-SN models E10, E12, E15, and E20 of HLW00 (a census of results is given in Table 6). As shown in Fig. 6, the trend identified for non-rotating progenitors holds qualitatively, but the results are quantitatively different. Going from 0.1, 0.3, 1.0, to 3.0 B explosion energies, we obtain increasing mean values of $V_{p,15d}$ of about 3000, 5000, 8000, and 14000 km s^{-1} , much larger than previously obtained. As expected, for a given main-sequence mass and explosion energy, the oxygen ejected in the SN II-P simulation reaches maximum speeds that are larger for rotating pre-SN models. For example, comparing the results for pre-SN models s15 and E15, we obtain $V_{e,O}$ of 730 and 1701 km s^{-1} , respectively (simulations s15e10m180v20 and E15e10m176v20). While a main-sequence mass limit of $\sim 20 M_{\odot}$ emerged for the representative value $V_{e,O} \sim 1000 \text{ km s}^{-1}$ in 1.0 B explosions of non-rotating SNe II-P progenitors, the allowance for rotation lowers this mass limit to $\sim 12 M_{\odot}$. Note that we are here addressing how rotation conditions the helium-core mass of a massive star and the signatures it leaves in a SN II-P ejecta; we are not considering how it may play a role in the explosion mechanism itself or how that initial angular momentum is eventually distributed in the star at the time of collapse.

4 DISCUSSION AND CONCLUSIONS

In this paper, we have presented results from radiation-hydrodynamics simulations of core-collapse SN explosions, using two sets of pre-SN progenitor models *evolved at solar metallicity* and accounting or not for stellar rotation (WHW02, HLW00). Our sample of objects includes stars that possess a sizeable hydrogen-rich envelope, die in their RSG stage, and produce a SN II-P. Because of mass loss, their final mass at the time of collapse is expected to be fairly degenerate although somewhat uncertain ($\lesssim 15 M_{\odot}$; WHW02). However, an important property of stellar structure and evolution is that stars with larger main-sequence mass possess more massive helium cores. The range in the non-rotating pre-SN models of WHW02 we employ is 1.75 to 9.18 M_{\odot} for main-sequence masses 11 to 30 M_{\odot} . Rotating stars achieve the same helium-core mass for lower main-sequence mass, so that a given helium-core mass can be used to set an upper limit to the main-sequence star mass. Because the objects in our sample have not been peeled off down to the helium core, the trend of increasing helium-core mass with increasing main-sequence mass is preserved. In this study, we quantified the asymptotic kinematic properties of SN II-P ejecta, and in particular searched for trends that would distinguish objects with a markedly different helium-core mass.

With our radiation-hydrodynamics simulations, we recover the trivial result that more energetic explosions lead to larger ejecta expansion rates, as visible from the velocities of various shells of the progenitor envelope, or by inspection of the photospheric velocity. However, we emphasise that for a *given* ejecta kinetic energy, pre-SN stars with a higher *main-sequence* mass yield SN ejecta with similar photospheric velocities but increasing velocities of helium-core material. One important element abundant in the helium-core is oxygen, and one important location is the outer edge of the oxygen-rich shell. For a standard-energy core-collapse

⁴ As we discuss in the appendix, this does not apply to the resulting remnant mass, which we find to be dramatically sensitive to the piston speed.

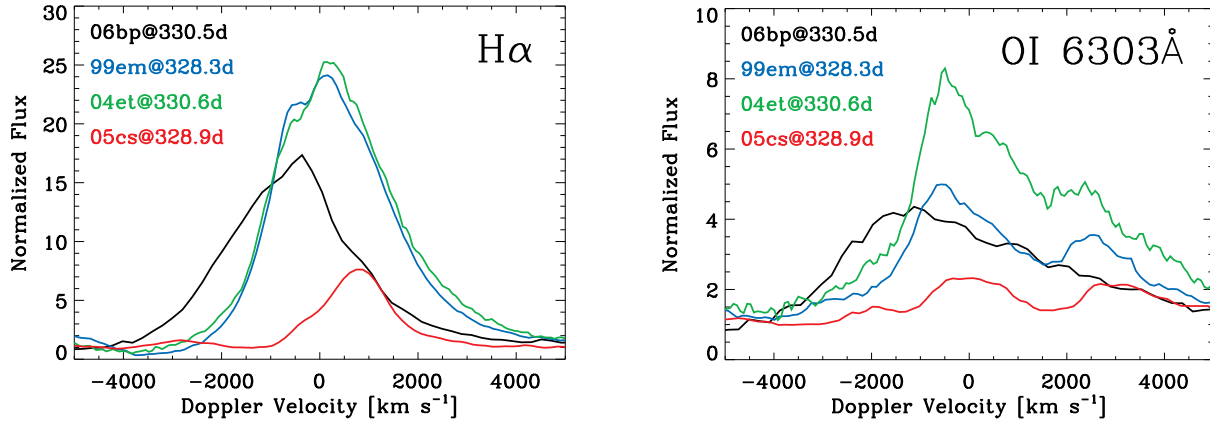


Figure 7. Illustration of the $H\alpha$ (left) and $O\text{I } 6303\text{--}6363\text{\AA}$ (right) line profiles versus Doppler velocity for four SNe II-P at about 300–350 d after explosion. Specifically, we show data for SN1999em (blue; Leonard et al. 2002; age of ~ 328 days) SN2004et (green; Sahu et al. 2006; age of ~ 303 d), SN2005cs (red; Pastorello et al. 2009; age of ~ 329 days) and SN2006bp (black; Quimby et al. 2007; age of ~ 330 d). The data has been de-redshifted using the redshift values quoted in those works, and shifted vertically to best render the profile widths. [See text for discussion].

SN explosion of 1 B, we find that the velocity of the outer edge of the oxygen-rich shell is smaller than $\sim 1000 \text{ km s}^{-1}$ for pre-SN stars with main-sequence mass smaller than $\sim 20 M_{\odot}$. Our 1D simulations based on *rotating* pre-SN models suggest that for the same ejecta kinetic energy, the same oxygen ejection speeds can be reached but for pre-SN stars with a lower main-sequence mass (for the last example, the mass threshold may be reduced down to $\sim 15 M_{\odot}$). All these results are shown in Figs. 4 and 6 and given in Tables 2–6. We find that tight constraints can be placed on the main-sequence mass of SN II-P progenitors based on two measurements, one of the photospheric velocity, which testifies for the strength of the explosion, and one of the velocity of the outer edge of the oxygen-rich shell, which testifies for the mass of the helium core and thus that of the star on the main sequence. Although potentially difficult to assess accurately on a case-by-case basis, the correlations identified above should emerge in observations of a *statistical* sample of SNe II-P in which under-energetic events are excluded to ensure some homogeneity. Combined with inferences based on light-curve modelling, which is sensitive to the properties of the hydrogen-envelope, but not to those of the helium core, one may better constrain the properties of the progenitor and of the explosion.

Inferences on ejecta kinematics can be done from line-profile morphology in spectroscopic observations. During the photospheric-phase of the SN, such measurements may be complicated by effects associated with line overlap, optical-depth (Dessart & Hillier 2005a), time-dependent effects (Dessart & Hillier 2008), ionisation (different lines are seen at distinct epochs, and these lines may be differentially affected by the previous two effects), or more generally the peculiarity of line-profile formation in SNe II (Dessart & Hillier 2005b). For example, Balmer lines in the early-time spectra of SN1987A yield a maximum P-Cygni absorption corresponding to a Doppler velocity that overestimates by up to a factor of two the contemporaneous photospheric velocity (Dessart & Hillier 2010). The ejecta kinetic energy of a SN II-P is best estimated at such early times when the photosphere is within the shock-heated hydrogen-rich part of the ejecta. The choice of 15 d after explosion, as above, is good - a later time during the photospheric phase is an alternative but

the measurement may then be influenced by multi-dimensional effects and decay heating. At late times in the nebular phase of the SN, such uncertainties are gone and one can simply measure the width of a line to assess the expansion velocity of the corresponding emitting region (this is best done for singlets and in the absence of line overlap). Such measurements have been performed on $O\text{I } 6303\text{--}6363\text{\AA}$ in SNe Ib/c to address the explosion energy and morphology, as well as the oxygen mass ejected (Modjaz et al. 2008; Tanaka et al. 2009; Taubenberger et al. 2009; Milisavljevic et al. 2010; Maurer et al. 2010).

Unfortunately, there exists only scant data on late-time spectra of SNe II-P, in particular extending out to 300 days after explosion, i.e. when the $O\text{I } 6303\text{--}6363\text{\AA}$ is well developed. These objects include SN1999em (Leonard et al. 2002), SN2004et (CfA archive; age of ~ 303 d), SN2005cs (Pastorello et al. 2009, age of ~ 329 days) and SN2006bp (Quimby et al. 2007, age of ~ 330 d), for which we show in Fig. 7 the observed (but rest-frame) $H\alpha$ (left) and $O\text{I } 6303\text{--}6363\text{\AA}$ (right) lines. The OI line is a doublet whose components appear well separated and narrower than the corresponding $H\alpha$ line, a result that is expected from the chemical stratification of the progenitor. Note however that if the explosion morphology was highly asymmetric, this relationship could be broken. We also note that the widths of the observed $H\alpha$ line varies from small (SN2005cs) to large (SNe 1999em and 2004et) and very large (SN2006bp). While $H\alpha$ appears quite symmetric with respect to line centre in SNe 1999em and 2004et, it is skewed to the blue in SN2006bp and to the red in SN2005cs.

Photospheric velocities of SNe 2005cs, 1999em, and 2006bp at 15 days after explosion have been inferred to be about 4700, 8800, and 10300 km s^{-1} (Dessart & Hillier 2006; Dessart et al. 2008a). Our simulations then suggest ejecta kinetic energies of $\sim 0.3 \text{ B}$ (Utrobin & Chugai 2008 obtain an explosion energy of $\sim 0.4 \text{ B}$), $\gtrsim 1.0 \text{ B}$ (Utrobin 2007 obtains an explosion energy of $\sim 1.3 \text{ B}$), and $\sim 2.0 \text{ B}$, respectively. Sahu et al. (2006) find that the spectral line profiles of SN2004et are somewhat larger than those of SN1999em at similar dates during their photospheric phase, which suggests that its explosion energy is larger than 1.0 B (Utrobin & Chugai 2009 obtain an ejecta kinetic energy of $\sim 2.3 \text{ B}$). Our estimates of the explosion energy based on $V_{p,15d}$ alone is

in good agreement with, although not a replacement of, such tailored radiation-hydrodynamics simulations. Using Figs. 4 and 6, together with the observations of the OI 6303–6363 Å line width as a guide, we can estimate a representative main-sequence mass of the progenitor. For SN2005cs, the low explosion energy prevents a good estimate although the very narrow half-width-at-half-maximum⁵ (HWHM) of $\sim 700 \text{ km s}^{-1}$ suggests the progenitor cannot be more massive than about $20 M_{\odot}$. For SN1999em, the HWHM of $\sim 1000 \text{ km s}^{-1}$ suggests a progenitor main-sequence mass on the order of $18 M_{\odot}$. For SN2004et, since it has a higher ejecta kinetic energy but a similar OI line-profile shape would suggest that its progenitor main-sequence mass is less than $\sim 18 M_{\odot}$. For SN2006bp, the skewness of the profile (both for OI and H α) suggests that the explosion may have been quite asymmetric or that dust is forming, scattering away the photons emitted from the receding part of the ejecta. From the large width of the OI line, we can however exclude a low-mass massive star as the progenitor. These predictions on main-sequence mass are compatible with those obtained from hydrodynamical simulations for SNe 2005cs and 1999em, but the relatively narrow OI 6303 Å line in the nebular spectrum of SN2004et argues against the high main-sequence mass proposed by Utrobin & Chugai (2009).⁶

Obviously, these inferences are not trivial and will require detailed radiative-transfer modelling. At present, given the scarcity of nebular-phase SNe II-P spectra, it seems difficult, and overly ambitious, to evaluate the accuracy of the method we present. However, we can identify two sources of uncertainty. The first is inherent to the simulations presented in this work and concerns the adequacy of the pre-SN models (e.g., with respect to mass loss), the potential role of multi-dimensional effects caused by an aspherical explosion and the mixing associated with Rayleigh-Taylor instabilities, the presence of stellar rotation etc. Inspection of Figs. 4 and 6 gives some measure of the sensitivity and uncertainty of the main-sequence mass corresponding to a set of $V_{e,O}$ and $V_{p,15d}$

⁵ An alternative is to consider the half-width at zero line flux (HWZF), in which case one obtains a larger estimate for the oxygen ejection speed and thus a larger estimate of the progenitor mass. However, this measurement is both imprecise and inaccurate. First, it is difficult to locate where the OI line flux goes to zero. Second, in such SNe II-P ejecta at ~ 300 d after explosion, the OI 6303–6363 Å region overlaps with FeII (as well as FeI) lines so that the flux seen in the wing of the OI 6303 Å line is corrupted by FeII-line flux (Dessart & Hillier, to be submitted). The easily-measured HWHM gets the bulk of the OI-line flux and represents a diagnostic less prone to errors. Furthermore, the HWZF will be relatively more sensitive to the effects of mixing, which leads to a spatial redistribution of the oxygen. Stronger mixing would likely produce a larger value of the HWZF, even for pre-SN progenitors with identical helium-cores

⁶ Given the analogous H α and OI profile shapes observed in SNe 1999em and 2004et, and the larger explosion energy inferred for the latter, our simulations support a lower or a comparable main-sequence mass for the SN2004et progenitor. Based exclusively on light-curve and photospheric-velocity modelling, Utrobin & Chugai (2009) propose a larger main-sequence mass of $25\text{--}29 M_{\odot}$, a much larger ejecta mass of $24.5 M_{\odot}$ (more than twice as large as our value for our simulations based on the s25–s30 pre-SN models, suggesting a surprisingly weak stellar-wind mass loss), a dense core of $\sim 2.5 M_{\odot}$ (their Fig. 1; note that the mass density should remain large out to the edge of the helium core at $8.1 M_{\odot}$, rather than dropping at a value of $\sim 2.5 M_{\odot}$). From Fig. 4 and this set of E_{kin} and M_1 , one reads a value of $V_{e,O}$ on the order of $2500\text{--}3000 \text{ km s}^{-1}$, which appears too large for the observed OI line. Their large initial-mass estimate is incompatible with our set of models for rotating massive stars evolved at solar metallicity, which explode as SNe Ib/c for $M_i \gtrsim 20 M_{\odot}$.

values. In the quoted mass estimates above, an uncertainty of a few solar masses seems to apply. Allowance for rotation will lead to a revision downward of the mass inferred from non-rotating models. The second is the validity of considering the width of the OI 6303–6363 Å doublet line as representative of the speed of the core-embedded oxygen-rich material ejected.⁷ This set of forbidden lines forms through collisional excitation and radiative de-excitation, a process that prevails when the ejecta density becomes on the order of 10^8 cm^{-3} . In their simulation of SN1987A, Kozma & Fransson (1998a,b) find that this line is thermally excited at nebular times up to ~ 500 d, and that it forms in the inner regions of the ejecta rich in Si/Ne/Mg/O/C. If this applies to SNe II-P at ~ 300 d too, it suggests that the OI line may not be strongly sensitive to the distribution and amount of ^{56}Ni , and that it should represent with fidelity the oxygen that was at the time of collapse in the helium core. We are aware of these complicated and important physical issues, but in this paper, we merely wish to emphasise the stiff dependence of $V_{e,O}$ with M_i , which, intuitively, should produce a clear signature in the width of the nebular phase OI 6303–6363 Å line. This correlation is an important part of the characterisation of SNe II-P progenitor and explosion properties, which should complement the inferences based on the modelling of the light curve and the photospheric velocity – it has so far been ignored. Importantly, more nebular-phase optical spectroscopic data of SNe II-P have to be gathered to build a statistical sample and investigate kinematics of the oxygen-rich ejected material. Furthermore, such a spectroscopic dataset would allow us to address the departures from spherical symmetry in the inner ejecta and the cumulative mass of oxygen ejected. Together with the knowledge of the helium-core mass, this would constrain the mass of the remnant and the magnitude of fallback, which are both very important for understanding the populations of stellar-mass compact objects and the chemical enrichment of galaxies.

All these issues can and need to be addressed quantitatively using high-quality photospheric- and nebular-phase SN II-P spectra/light-curves, and non-LTE time-dependent radiative-transfer simulations, with allowance for non-thermal excitation/ionisation, and based on physically-consistent hydrodynamical inputs of SN II-P ejecta. This is key for providing observational constraints on the way a generic massive star explodes and the properties of the remnant star left behind.

APPENDIX A: ADDITIONAL RESULTS

In this appendix, we present additional results from our simulations. These are placed here not to divert the main results we wanted to focus on, namely the ejecta kinematics and the associated chemical stratification. Furthermore, some of these results have already been discussed directly or indirectly (Falk & Arnett 1977; Baklanov et al. 2005; Utrobin 2007; Kasen & Woosley 2009; Woosley & Weaver 1995; Woosley et al. 2002; Zhang et al. 2008).

We give a log of the parameters and the main results of our simulations in Tables 2–6. For each entry (i.e. simulation name), we first give the simulation parameters, i.e. the initial model mass on the main sequence (M_i), the energy deposited by the pis-

⁷ We note that the minimum velocity of the hydrogen material inferred from H I Balmer lines could be used in combination to this OI-line measurement to make the interpretation more secure.

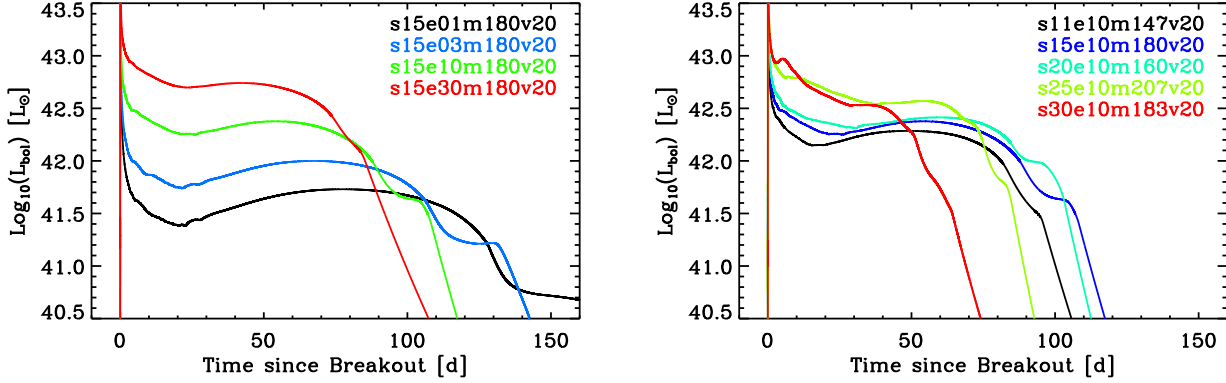


Figure A1. Evolution of the bolometric luminosity for the first 160 days for a variety of V1D simulations. In the left panel, we show our results for s15e01m180v20 (black), s15e03m180v20 (blue), s15e10m180v20 (green), and s15e30m180v20 (red), i.e. simulations that were started from the WHW02 pre-SN model s15 and exploded to yield and ejecta energy of 0.1, 0.3, 1.0, and 3.0 B. In the right panel, we show the result for an ejecta-kinetic energy of 1.0 B, but now for five different WHW02 pre-SN models, i.e. s11, s15, s20, s25, and s30.

ton (E_{kin}),⁸ the Lagrangian mass where the piston is positioned (M_{piston}), and the velocity of the piston (V_{piston}). We then give the final mass of the pre-SN star (M_f), the mass of the compact remnant (M_{remnant} , which corresponds to all the material that fails to eject), and the mass of the ejecta (M_{ejecta} , which is just $M_f - M_{\text{remnant}}$). Further, we provide information on the ejecta kinematics, with the mass-weighted mean velocity of the inner $0.1 M_\odot$ in the SN ejecta (V_{inner}), the velocity at the outer (inner) edge of the oxygen (hydrogen) shell $V_{\text{e,O}}$ ($V_{\text{i,H}}$), the photospheric velocity at 15 and 50 d after shock breakout ($V_{\text{p,15d}}$ and $V_{\text{p,50d}}$). We then give the asymptotic ejecta kinetic energy (e_{kt} , which may differ from E_{kin}), the fraction of e_{kt} that resides in the hydrogen-rich envelope (e_{kfH} ; it is close to 99% for low-mass massive stars but decreases for objects with increasing helium-core masses). Generally, the entire hydrogen-rich and helium-rich shells are ejected in our simulations for any of our adopted explosion energies and piston characteristics. However, the oxygen-rich shell suffers dramatically from fallback for low explosion energies and/or piston speeds and thus the total oxygen yield is given in the table to show this dependence. This correlates directly with the remnant mass given in the 7th column. Finally, we give two important times that characterise the light curve. First, the SN display is born at the shock-breakout time. We thus give here the delay time between the piston trigger and the shock breakout time t_{SBO} . We also give the plateau duration Δt_P (defined as the post-breakout time when the luminosity has decreased to a tenth of the plateau-peak value). Note that no ^{56}Ni is present in our simulations, so that the plateau duration is a lower limit to what it can be. We show a sample of bolometric-light curves obtained in our simulations in Fig. A1, both for a given pre-SN model exploded with various explosion energies (left panel), and for a range of pre-SN models exploded with a given explosion energy (right panel). Our results for the plateau brightness and duration are in good agreement, for example, with the results of Kasen & Woosley (2009). We defer a thorough discussion of SNe II-P radiative properties to a separate study based on more detailed

non-LTE time-dependent simulations, including both spectra and light curves, and covering the photospheric to the nebular phase (Dessart & Hillier, to be submitted).

In Fig A2, using all the V1D simulations presented above, we show our results for important reference masses. As a function of main-sequence mass for our sample of pre-SN progenitor stars, we show the final star mass at collapse M_f (red; dots indicate the initial masses of the individual models effectively calculated), the Lagrangian mass coordinate corresponding to the inner edge of the hydrogen shell ($M_{\text{i,H}}$, turquoise), to the outer edge of the helium core ($M_{\text{e,He}}$, blue), to the outer edge of the oxygen-rich shell ($M_{\text{e,O}}$, orange), and to the outer edge of the iron core (M_{core} , violet). Notice again the monotonic increase of $M_{\text{i,H}}$, $M_{\text{e,He}}$, $M_{\text{e,O}}$, as a function of main-sequence mass. Now, overplotted, we draw black curves (separated by hatched regions of differing orientations) for the remnant mass obtained for each pre-SN progenitor model exploded with an energy of 0.1 B (top black curve), 0.3 B (black curve second from top), 1.0 B (black curve third from top), and 3.0 B (bottom black curve). The piston speed is 10000 km s^{-1} (20000 km s^{-1}) for simulations shown in the left (right) panel. Whatever the piston speed, we find that low-energy explosions suffer a large fallback, whose magnitude increases with pre-SN model main-sequence mass. For example, if all SNe II-P exploded with an energy of 0.1 B or less, no oxygen from the helium core would be ejected, and the helium core would collapse into the neutron star or in the black hole. In many cases, despite the successful, albeit somewhat weak, explosion, a large fraction of the core would fail to escape. For large-energy explosions, our choice of piston speed is not as important and little fallback occurs. However, for a standard-energy core-collapse SN explosion of 1.0 B, the amount of fallback is highly dependent on our choice of piston speed, which sets the timescale over which the energy is deposited, as well as the strength of the shock. As the shock traverses the helium-core, the slowly decreasing density slows it down considerably, so that insufficient energy may be imparted to those deep envelope layers. Furthermore, when the SN shock reaches the interface between the hydrogen-rich and helium-rich shells, a reverse shock forms and slows down these inner regions even further. Together, these two effects tend to lead to larger fallback masses for increasing helium-core masses (Herant & Woosley 1994; Zhang et al. 2008). The dependency on the piston speed is in-

⁸ As pointed out earlier, this corresponds to the ejecta kinetic energy at infinity when the explosion is large, but for low-energy explosions, the large fallback mass tends to lead to an overestimate of the energy aimed for. The 14th column gives the kinetic energy the ejecta effectively have asymptotically.

teresting because it constrains the timescale for the explosion. Determining observationally the explosion energy, the main-sequence mass and the remnant mass in a given SN could thus potentially give a measure of the explosion timescale and constrain the explosion mechanism.

Using spectroscopic observations and detailed radiative-transfer calculations based on hydrodynamical models of SN II-P explosions should allow one to address these issues. The photospheric velocity at 15 d after shock breakout sets a constraint on the explosion energy. The maximum velocity of the oxygen-rich material, inferred from nebular spectra using the OI 6303–6363 Å doublet line, gives a measure of the maximum velocity at which the outer helium core has been ejected, which constrains the helium-core mass of the progenitor star (and thus its main-sequence mass). Finally, quantitative spectroscopy on the formation of the OI 6303–6363 Å doublet line when the ejecta is fully optically thin can determine how much oxygen was effectively ejected. This constrains the fraction of the core that was ejected and thus the remnant mass.

REFERENCES

- Akiyama, S., Wheeler, J. C., Meier, D. L., & Lichtenstadt, I. 2003, *ApJ*, 584, 954
- Arnett, D. 1991, in *Astronomical Society of the Pacific Conference Series*, Vol. 20, *Frontiers of Stellar Evolution*, ed. D. L. Lambert, 389–401
- Baklanov, P. V., Blinnikov, S. I., & Pavlyuk, N. N. 2005, *Astronomy Letters*, 31, 429
- Bersten, M. C. & Hamuy, M. 2009, *ApJ*, 701, 200
- Bisnovatyi-Kogan, G. S., Popov, I. P., & Samokhin, A. A. 1976, *Ap&SS*, 41, 287
- Burrows, A., Dessart, L., Livne, E., Ott, C. D., & Murphy, J. 2007a, *ApJ*, 664, 416
- Burrows, A., Livne, E., Dessart, L., Ott, C. D., & Murphy, J. 2006, *ApJ*, 640, 878
- . 2007b, *ApJ*, 655, 416
- Cantiello, M., Yoon, S., Langer, N., & Livio, M. 2007, *A&A*, 465, L29
- de Jager, C., Nieuwenhuijzen, H., & van der Hucht, K. A. 1988, *A&AS*, 72, 259
- Dessart, L., Blondin, S., Brown, P. J., Hicken, M., Hillier, D. J., Holland, S. T., Immler, S., Kirshner, R. P., Milne, P., Modjaz, M., & Roming, P. W. A. 2008a, *ApJ*, 675, 644
- Dessart, L., Burrows, A., Livne, E., & Ott, C. D. 2008b, *ApJL*, 673, L43
- Dessart, L. & Hillier, D. J. 2005a, *A&A*, 439, 671
- . 2005b, *A&A*, 437, 667
- . 2006, *A&A*, 447, 691
- . 2008, *MNRAS*, 383, 57
- . 2010, *MNRAS*, 572, arXiv:1003.2557
- Dessart, L., Livne, E., & Waldman, R. 2010, *MNRAS*, 585, arXiv:0910.3655
- Falk, S. W. & Arnett, W. D. 1977, *ApJS*, 33, 515
- Hammer, N. J., Janka, H., & Mueller, E. 2009, *ArXiv e-prints*
- Hamuy, M. 2003, *ApJ*, 582, 905
- Heger, A., Jeannin, L., Langer, N., & Baraffe, I. 1997, *A&A*, 327, 224
- Heger, A., Langer, N., & Woosley, S. E. 2000, *ApJ*, 528, 368
- Heger, A. & Woosley, S. E. 2008, *ArXiv e-prints*
- Herant, M., Benz, W., Hix, W. R., Fryer, C. L., & Colgate, S. A. 1994, *ApJ*, 435, 339
- Herant, M. & Woosley, S. E. 1994, *ApJ*, 425, 814
- Joggerst, C. C., Almgren, A., Bell, J., Heger, A., Whalen, D., & Woosley, S. E. 2010, *ApJ*, 709, 11
- Josselin, E. & Plez, B. 2007, *A&A*, 469, 671
- Kasen, D. & Woosley, S. E. 2009, *ApJ*, 703, 2205
- Kifonidis, K., Plewa, T., Janka, H., & Müller, E. 2000, *ApJL*, 531, L123
- . 2003, *A&A*, 408, 621
- Kifonidis, K., Plewa, T., Scheck, L., Janka, H., & Müller, E. 2006, *A&A*, 453, 661
- Kozma, C. & Fransson, C. 1998a, *ApJ*, 496, 946
- . 1998b, *ApJ*, 497, 431
- LeBlanc, J. M. & Wilson, J. R. 1970, *ApJ*, 161, 541
- Leonard, D. C., Filippenko, A. V., Gates, E. L., Li, W., Eastman, R. G., Barth, A. J., Bus, S. J., Chornock, R., Coil, A. L., Frink, S., Grady, C. A., Harris, A. W., Malkan, M. A., Matheson, T., Quirrenbach, A., & Treffers, R. R. 2002, *PASP*, 114, 35
- Li, W., Van Dyk, S. D., Filippenko, A. V., Cuillandre, J., Jha, S., Bloom, J. S., Riess, A. G., & Livio, M. 2006, *ApJ*, 641, 1060
- Livne, E. 1993, *ApJ*, 412, 634
- Marek, A. & Janka, H. 2009, *ApJ*, 694, 664
- Mattila, S., Smartt, S. J., Eldridge, J. J., Maund, J. R., Crockett, R. M., & Danziger, I. J. 2008, *ApJL*, 688, L91
- Maund, J. R., Smartt, S. J., & Danziger, I. J. 2005, *MNRAS*, 364, L33
- Maurer, J. I., Mazzali, P. A., Deng, J., Filippenko, A. V., Hamuy, M., Kirshner, R. P., Matheson, T., Modjaz, M., Pian, E., Stritzinger, M., Taubenberger, S., & Valenti, S. 2010, *MNRAS*, 402, 161
- Meynet, G., Ekström, S., & Maeder, A. 2006, *A&A*, 447, 623
- Milisavljevic, D., Fesen, R. A., Gerardy, C. L., Kirshner, R. P., & Challis, P. 2010, *ApJ*, 709, 1343
- Modjaz, M., Kirshner, R. P., Blondin, S., Challis, P., & Matheson, T. 2008, *ApJL*, 687, L9
- Moiseenko, S. G., Bisnovatyi-Kogan, G. S., & Ardeljan, N. V. 2006, *MNRAS*, 370, 501
- Mueller, E., Fryxell, B., & Arnett, D. 1991, *A&A*, 251, 505
- Nadyozhin, D. K. 2003, *MNRAS*, 346, 97
- O’Connor, E. & Ott, C. D. 2010, *Classical and Quantum Gravity*, 27, 114103
- Pastorello, A., Valenti, S., Zampieri, L., Navasardyan, H., Taubenberger, S., Smartt, S. J., Arkharov, A. A., Bärnbantner, O., Barwig, H., Benetti, S., Birtwhistle, P., Botticella, M. T., Cappellaro, E., Del Principe, M., di Mille, F., di Rico, G., Dolci, M., Elias-Rosa, N., Efimova, N. V., Fiedler, M., Harutyunyan, A., Höflich, P. A., Kloeher, W., Larionov, V. M., Lorenzi, V., Maund, J. R., Napoleone, N., Ragni, M., Richmond, M., Ries, C., Spiro, S., Temporin, S., Turatto, M., & Wheeler, J. C. 2009, *MNRAS*, 394, 2266
- Popov, D. V. 1993, *ApJ*, 414, 712
- Quimby, R. M., Wheeler, J. C., Höflich, P., Akerlof, C. W., Brown, P. J., & Rykoff, E. S. 2007, *ApJ*, 666, 1093
- Sahu, D. K., Anupama, G. C., Srividya, S., & Muneer, S. 2006, *MNRAS*, 372, 1315
- Smartt, S. J. 2009, *ARA&A*, 47, 63
- Smartt, S. J., Maund, J. R., Hendry, M. A., Tout, C. A., Gilmore, G. F., Mattila, S., & Benn, C. R. 2004, *Science*, 303, 499
- Smith, N., Hinkle, K. H., & Ryde, N. 2009, *AJ*, 137, 3558
- Symbolist, E. M. D. 1984, *ApJ*, 285, 729
- Taam, R. E. & Ricker, P. M. 2006, *ArXiv Astrophysics e-prints*
- Tanaka, M., Yamanaka, M., Maeda, K., Kawabata, K. S., Hattori, T., Minezaki, T., Valenti, S., Della Valle, M., Sahu, D. K., Anu-

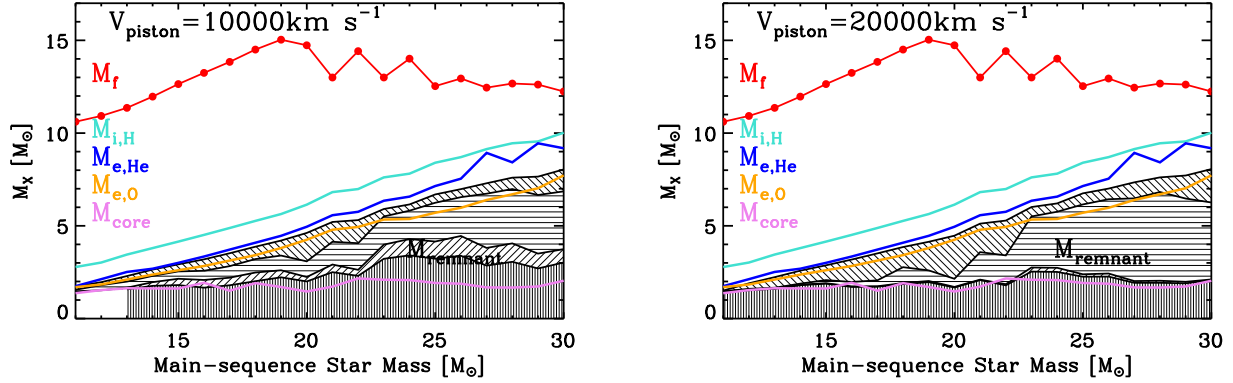


Figure A2. Illustration as a function of main-sequence mass of several important reference mass coordinates, characterising both the pre-SN models of WHW02 as well as their resulting ejecta, produced with `v1D` using a piston speed of 10000 km s^{-1} (left) or 20000 km s^{-1} (right). The black curves limiting from above the hatched regions with stripe orientation at -45° , 0° , 45° , and 90° correspond to models with asymptotic ejecta kinetic energy of 0.1, 0.3, 1.0, and 3.0 B (models yield monotonically increasing remnant masses for decreasing explosion energies). We over-plot key quantities characterising the structure of the progenitor model (prior to core-collapse and explosion), such as the final mass (red line), the Lagrangian mass at the base of the hydrogen shell (turquoise), at the outer edge of the helium/oxygen shell (blue/orange), and the Lagrangian mass at the iron-core edge (violet). For ejecta kinetic energy on the order of 0.1 B, the entire highly-bound helium-core falls back: Neither nuclear-processed oxygen nor unstable isotopes would be copiously ejected. Note that the two simulations based on the pre-SN models s11 and s12, and characterised by an explosion energy of 3.0 B, and a piston speed of 10000 km s^{-1} , are not plotted since with such a slow piston speed they reach this large explosion energy on an unphysically long timescale of minutes (they are also omitted from Table 2). [See text for discussion].

pama, G. C., Tominaga, N., Nomoto, K., Mazzali, P. A., & Pian, E. 2009, *ApJ*, 700, 1680

Taubenberger, S., Valenti, S., Benetti, S., Cappellaro, E., Della Valle, M., Elias-Rosa, N., Hachinger, S., Hillebrandt, W., Maeda, K., Mazzali, P. A., Pastorello, A., Patat, F., Sim, S. A., & Turatto, M. 2009, *MNRAS*, 397, 677

Tominaga, N. 2009, *ApJ*, 690, 526

Tominaga, N., Maeda, K., Umeda, H., Nomoto, K., Tanaka, M., Iwamoto, N., Suzuki, T., & Mazzali, P. A. 2007, *ApJL*, 657, L77

Utrobin, V. P. 2007, *A&A*, 461, 233

Utrobin, V. P. & Chugai, N. N. 2008, *A&A*, 491, 507

—. 2009, *A&A*, 506, 829

Uzdensky, D. A. & MacFadyen, A. I. 2007, *ApJ*, 669, 546

Van Dyk, S. D., Li, W., & Filippenko, A. V. 2003, *PASP*, 115, 1289

Weaver, T. A. & Woosley, S. E. 1979, in *Bulletin of the American Astronomical Society*, Vol. 11, *Bulletin of the American Astronomical Society*, 724–+

Weinberg, N. N. & Quataert, E. 2008, *MNRAS*, 387, L64

Woosley, S. E., Heger, A., & Weaver, T. A. 2002, *Reviews of Modern Physics*, 74, 1015

Woosley, S. E. & Weaver, T. A. 1995, *ApJS*, 101, 181

Yoon, S. & Cantiello, M. 2010, *arXiv:1005.4925*

Zhang, W., Woosley, S. E., & Heger, A. 2008, *ApJ*, 679, 639

Table 2. Summary of properties for our simulations based on the non-rotating pre-SN models of WHW02 with main-sequence mass in the range 11-15 M_{\odot} . For each, we give the asymptotic ejecta kinetic energy aimed for E_{kin} , the mass of the remnant M_{remnant} (i.e. the material that fails to escape and accumulates in the neutron star or black hole), the mass of the ejecta M_{ejecta} , the mean velocity of the inner 0.1 M_{\odot} of the ejecta V_{inner} , the velocity at the outer (inner) edge of the oxygen (hydrogen) shell $V_{\text{e,O}}$ ($V_{\text{i,H}}$), the photospheric velocity at 15 d (50 d) after shock breakout $V_{\text{p,15d}}$ ($V_{\text{p,50d}}$), the ejected oxygen mass M_{O} , the delay time between the piston trigger and shock breakout t_{SBO} , and the plateau duration Δt_P (defined as the time it takes the luminosity to decrease after the plateau peak by a factor of 10; note that no ^{56}Ni is injected in the ejecta, so that this plateau duration is a lower limit).

Simulation Name	M_{i} [M_{\odot}]	E_{kin} [B]	M_{piston} [M_{\odot}]	V_{piston} [km s^{-1}]	M_{f} [M_{\odot}]	M_{remnant} [M_{\odot}]	M_{ejecta} [M_{\odot}]	V_{inner} [km s^{-1}]	$V_{\text{e,O}}$ [km s^{-1}]	$V_{\text{i,H}}$ [km s^{-1}]	$V_{\text{p,15d}}$ [km s^{-1}]	$V_{\text{p,50d}}$ [km s^{-1}]	e_{kt} [B]	e_{kFH} %	M_{O} [M_{\odot}]	t_{SBO} [d]	Δt_P [d]
s11e01m147v10	11.0	0.1	1.47	10000	10.61	1.73	8.88	173	103	328	2931	1405	0.11	99	0.1029	3.0	144.2
s11e01m147v20	11.0	0.1	1.47	20000	10.61	1.52	9.09	142	180	290	2912	1397	0.11	99	0.2400	3.0	151.8
s11e03m147v10	11.0	0.3	1.47	10000	10.61	1.55	9.05	225	285	532	4770	2113	0.30	99	0.2188	1.9	121.7
s11e03m147v20	11.0	0.3	1.47	20000	10.61	1.47	9.13	250	315	526	4774	2128	0.31	99	0.2633	1.9	123.3
s11e10m147v10	11.0	1.0	1.47	10000	10.61	1.47	9.13	375	493	920	8096	3329	0.99	99	0.2633	1.0	97.0
s11e10m147v20	11.0	1.0	1.47	20000	10.61	1.47	9.13	452	590	963	8198	3354	1.00	99	0.2633	1.0	97.1
s11e30m147v20	11.0	3.0	1.47	20000	10.61	1.47	9.13	706	930	1645	12957	4838	2.99	99	0.2633	0.6	81.9
s12e01m152v10	12.0	0.1	1.52	10000	10.92	1.96	8.96	182	144	351	3148	1514	0.13	99	0.0769	3.1	143.9
s12e01m152v20	12.0	0.1	1.52	20000	10.92	1.90	9.02	153	153	324	3077	1488	0.12	99	0.1146	3.2	146.2
s12e03m152v10	12.0	0.3	1.52	10000	10.92	1.80	9.12	246	316	542	4832	2197	0.32	99	0.1897	2.0	125.0
s12e03m152v20	12.0	0.3	1.52	20000	10.92	1.60	9.32	250	354	499	4808	2203	0.32	99	0.3191	2.0	127.7
s12e10m152v10	12.0	1.0	1.52	10000	10.92	1.52	9.40	411	605	870	8109	3418	0.99	99	0.3639	1.2	101.6
s12e10m152v20	12.0	1.0	1.52	20000	10.92	1.55	9.37	436	668	911	8189	3428	1.01	99	0.3519	1.1	100.9
s12e30m152v20	12.0	3.0	1.52	20000	10.92	1.52	9.40	759	1115	1530	13398	4925	2.99	99	0.3639	0.7	83.7
s13e01m157v10	13.0	0.1	1.57	10000	11.36	2.29	9.07	168	141	333	3067	1603	0.13	99	0.0849	3.4	143.6
s13e01m157v20	13.0	0.1	1.57	20000	11.36	2.23	9.13	153	162	325	2995	1569	0.13	99	0.1252	3.5	144.7
s13e03m157v10	13.0	0.3	1.57	10000	11.36	1.99	9.36	227	337	470	4757	2296	0.32	99	0.2974	2.2	132.4
s13e03m157v20	13.0	0.3	1.57	20000	11.36	1.66	9.69	223	368	519	4666	2278	0.31	99	0.5209	2.3	128.6
s13e10m157v10	13.0	1.0	1.57	10000	11.36	1.66	9.69	412	673	940	7866	3552	1.00	99	0.5209	1.3	102.3
s13e10m157v20	13.0	1.0	1.57	20000	11.36	1.61	9.75	408	686	914	7894	3521	1.01	99	0.5480	1.3	103.3
s13e30m157v10	13.0	3.0	1.57	10000	11.36	1.57	9.78	526	851	1193	13628	4728	2.99	99	0.5564	0.8	84.5
s13e30m157v20	13.0	3.0	1.57	20000	11.36	1.61	9.75	722	1206	1609	13126	5049	3.00	99	0.5492	0.8	84.5
s14e01m176v10	14.0	0.1	1.76	10000	11.97	2.64	9.32	165	145	324	3087	1666	0.14	99	0.0703	3.7	145.1
s14e01m176v20	14.0	0.1	1.76	20000	11.97	2.59	9.38	135	124	281	2939	1602	0.13	99	0.0975	3.9	147.8
s14e03m176v10	14.0	0.3	1.76	10000	11.97	2.30	9.66	219	325	449	4719	2375	0.32	99	0.3013	2.5	138.2
s14e03m176v20	14.0	0.3	1.76	20000	11.97	1.88	10.08	206	368	520	4573	2338	0.31	99	0.5948	2.6	132.3
s14e10m176v10	14.0	1.0	1.76	10000	11.97	1.96	10.00	388	658	909	7963	3686	1.00	99	0.5386	1.4	106.4
s14e10m176v20	14.0	1.0	1.76	20000	11.97	1.83	10.13	402	684	900	7930	3658	1.01	99	0.6314	1.5	106.8
s14e30m176v10	14.0	3.0	1.76	10000	11.97	1.76	10.20	588	981	1306	12903	5006	2.99	99	0.6811	0.9	88.6
s14e30m176v20	14.0	3.0	1.76	20000	11.97	1.80	10.17	693	1233	1617	12705	5272	3.00	98	0.6560	0.9	87.1
s15e01m180v10	15.0	0.1	1.80	10000	12.64	2.92	9.72	176	150	339	3228	1796	0.16	99	0.0850	3.8	145.5
s15e01m180v20	15.0	0.1	1.80	20000	12.64	2.87	9.77	155	155	324	3087	1730	0.15	99	0.1146	4.0	145.4
s15e03m180v10	15.0	0.3	1.80	10000	12.64	2.54	10.10	229	338	476	4584	2451	0.34	99	0.3527	2.7	140.9
s15e03m180v20	15.0	0.3	1.80	20000	12.64	2.07	10.57	191	396	542	4455	2406	0.32	98	0.6734	2.8	135.4
s15e10m180v10	15.0	1.0	1.80	10000	12.64	2.15	10.49	364	676	904	7581	3767	1.01	99	0.6236	1.6	109.4
s15e10m180v20	15.0	1.0	1.80	20000	12.64	1.91	10.73	383	730	927	7485	3736	1.02	98	0.7905	1.6	108.5
s15e30m180v10	15.0	3.0	1.80	10000	12.64	1.80	10.84	624	1169	1501	12370	5249	2.98	98	0.8658	1.0	88.7
s15e30m180v20	15.0	3.0	1.80	20000	12.64	1.88	10.76	670	1308	1652	12489	5387	3.01	98	0.8075	0.9	88.7

Table 3. Same as Table 2, but now for the non-rotating pre-SN models of WHW02 with a main-sequence mass in the range 16–20 M_{\odot} .

Simulation Name	M_i [M_{\odot}]	E_{kin} [B]	M_{piston} [M_{\odot}]	V_{piston} [km s $^{-1}$]	M_f [M_{\odot}]	M_{remnant} [M_{\odot}]	M_{ejecta} [M_{\odot}]	V_{inner} [km s $^{-1}$]	$V_{\text{e,O}}$ [km s $^{-1}$]	$V_{\text{i,H}}$ [km s $^{-1}$]	$V_{\text{p,15d}}$ [km s $^{-1}$]	$V_{\text{p,50d}}$ [km s $^{-1}$]	ϵ_{kt} [B]	ϵ_{kfH} %	M_{O} [M_{\odot}]	t_{SBO} [d]	Δt_P [d]
s16e01m163v10	16.0	0.1	1.63	10000	13.24	3.19	10.05	168	177	333	3238	1870	0.17	99	0.1289	4.1	143.8
s16e01m163v20	16.0	0.1	1.63	20000	13.24	3.18	10.06	139	150	257	3067	1781	0.15	99	0.1366	4.3	143.4
s16e03m163v10	16.0	0.3	1.63	10000	13.24	2.58	10.67	215	363	512	4402	2521	0.34	99	0.5627	2.9	140.5
s16e03m163v20	16.0	0.3	1.63	20000	13.24	1.97	11.27	139	450	588	4206	2447	0.32	98	0.9605	3.1	135.0
s16e10m163v10	16.0	1.0	1.63	10000	13.24	2.08	11.16	334	782	984	7475	3869	1.02	98	0.8886	1.8	109.9
s16e10m163v20	16.0	1.0	1.63	20000	13.24	1.74	11.51	363	851	1024	7335	3810	1.02	98	1.0058	1.8	108.0
s16e30m163v10	16.0	3.0	1.63	10000	13.24	1.67	11.58	647	1448	1768	11427	5489	2.98	98	1.0106	1.1	88.4
s16e30m163v20	16.0	3.0	1.63	20000	13.24	1.70	11.54	630	1496	1775	11694	5483	3.00	98	1.0080	1.1	89.4
s17e01m165v10	17.0	0.1	1.65	10000	13.84	3.52	10.31	147	165	299	3125	1890	0.17	99	0.1439	4.3	143.1
s17e01m165v20	17.0	0.1	1.65	20000	13.84	3.51	10.32	149	172	302	2994	1808	0.15	99	0.1497	4.5	144.9
s17e03m165v10	17.0	0.3	1.65	10000	13.84	2.83	11.01	193	370	507	4268	2515	0.33	99	0.6323	3.2	141.9
s17e03m165v20	17.0	0.3	1.65	20000	13.84	2.06	11.77	150	481	602	4116	2457	0.32	98	1.1406	3.3	136.0
s17e10m165v10	17.0	1.0	1.65	10000	13.84	2.20	11.63	307	829	1006	7090	3886	1.01	98	1.0458	1.9	110.8
s17e10m165v20	17.0	1.0	1.65	20000	13.84	1.74	12.09	341	913	1061	6878	3819	1.01	97	1.2099	2.0	108.6
s17e30m165v10	17.0	3.0	1.65	10000	13.84	1.80	12.04	601	1564	1840	11418	5606	2.98	97	1.2015	1.1	90.0
s17e30m165v20	17.0	3.0	1.65	20000	13.84	1.72	12.11	598	1601	1834	11549	5525	3.00	97	1.2129	1.1	90.3
s18e01m172v10	18.0	0.1	1.72	10000	14.50	3.87	10.63	163	189	330	3376	2055	0.20	99	0.1630	4.2	142.1
s18e01m172v20	18.0	0.1	1.72	20000	14.50	3.86	10.64	148	172	258	3192	1945	0.18	99	0.1718	4.5	144.9
s18e03m172v10	18.0	0.3	1.72	10000	14.50	3.21	11.29	193	351	479	4437	2651	0.37	99	0.6281	3.2	145.7
s18e03m172v20	18.0	0.3	1.72	20000	14.50	2.79	11.71	108	416	535	4296	2553	0.34	98	0.9077	3.4	140.8
s18e10m172v10	18.0	1.0	1.72	10000	14.50	2.48	12.02	268	828	993	7225	3979	1.03	98	1.1089	2.0	113.0
s18e10m172v20	18.0	1.0	1.72	20000	14.50	1.91	12.59	349	945	1082	6984	3908	1.02	97	1.4875	2.1	110.2
s18e30m172v10	18.0	3.0	1.72	10000	14.50	2.02	12.48	575	1606	1850	11371	5727	2.99	97	1.4202	1.2	92.0
s18e30m172v20	18.0	3.0	1.72	20000	14.50	1.86	12.64	591	1633	1840	11552	5624	3.00	97	1.4910	1.2	92.0
s19e01m189v10	19.0	0.1	1.89	10000	15.03	4.22	10.81	102	139	250	3151	1965	0.18	99	0.1612	4.6	143.4
s19e01m189v20	19.0	0.1	1.89	20000	15.03	4.14	10.89	138	173	234	3009	1882	0.16	99	0.2123	4.8	146.3
s19e03m189v10	19.0	0.3	1.89	10000	15.03	3.40	11.63	146	374	487	4167	2618	0.35	99	0.7498	3.5	144.5
s19e03m189v20	19.0	0.3	1.89	20000	15.03	2.60	12.44	154	489	596	4051	2575	0.34	98	1.3242	3.6	139.7
s19e10m189v10	19.0	1.0	1.89	10000	15.03	2.60	12.43	280	861	1004	6861	4002	1.02	98	1.3187	2.1	114.2
s19e10m189v20	19.0	1.0	1.89	20000	15.03	2.03	13.01	352	975	1093	6722	3957	1.02	97	1.7428	2.2	110.9
s19e30m189v10	19.0	3.0	1.89	10000	15.03	2.22	12.81	553	1650	1866	11162	5840	2.99	97	1.5961	1.3	93.1
s19e30m189v20	19.0	3.0	1.89	20000	15.03	1.97	13.07	570	1678	1854	11330	5673	3.00	97	1.7887	1.3	92.6
s20e01m160v10	20.0	0.1	1.60	10000	14.73	4.67	10.06	74	137	260	2957	1923	0.15	99	0.1815	5.2	141.1
s20e01m160v20	20.0	0.1	1.60	20000	14.73	4.47	10.26	130	166	260	2901	1886	0.15	99	0.3152	5.3	157.3
s20e03m160v10	20.0	0.3	1.60	10000	14.73	3.08	11.65	176	525	624	4046	2634	0.32	97	1.2593	3.8	137.0
s20e03m160v20	20.0	0.3	1.60	20000	14.73	2.15	12.58	216	607	701	3984	2584	0.32	96	1.8866	3.9	133.8
s20e10m160v10	20.0	1.0	1.60	10000	14.73	2.24	12.49	407	1106	1230	6848	4086	1.00	96	1.8223	2.3	107.8
s20e10m160v20	20.0	1.0	1.60	20000	14.73	1.71	13.02	452	1212	1317	6741	4000	1.00	95	2.1223	2.4	104.8
s20e30m160v10	20.0	3.0	1.60	10000	14.73	2.00	12.73	716	2000	2181	11251	5966	2.98	96	1.9829	1.3	89.7
s20e30m160v20	20.0	3.0	1.60	20000	14.73	1.67	13.06	783	2048	2200	11266	5723	2.99	95	2.1277	1.4	88.0

Table 4. Same as Table 2, but now for the non-rotating pre-SN models of WHW02 with a main-sequence mass in the range 21–25 M_{\odot}

Simulation Name	M_i [M_{\odot}]	E_{kin} [B]	M_{piston} [M_{\odot}]	V_{piston} [km s $^{-1}$]	M_f [M_{\odot}]	M_{remnant} [M_{\odot}]	M_{ejecta} [M_{\odot}]	V_{inner} [km s $^{-1}$]	$V_{\text{e,O}}$ [km s $^{-1}$]	$V_{\text{i,H}}$ [km s $^{-1}$]	$V_{\text{p,15d}}$ [km s $^{-1}$]	$V_{\text{p,50d}}$ [km s $^{-1}$]	ϵ_{kt} [B]	ϵ_{kfH} %	M_{O} [M_{\odot}]	t_{SBO} [d]	Δt_P [d]
s21e01m193v10	21.0	0.1	1.93	10000	13.00	5.21	7.79	164	268	453	3601	2468	0.20	99	0.2319	4.4	137.3
s21e01m193v20	21.0	0.1	1.93	20000	13.00	5.12	7.88	206	319	465	3434	2360	0.18	98	0.2872	4.6	149.0
s21e03m193v10	21.0	0.3	1.93	10000	13.00	4.14	8.86	254	676	830	4574	3118	0.36	97	0.9804	3.5	118.8
s21e03m193v20	21.0	0.3	1.93	20000	13.00	3.58	9.41	278	731	871	4454	3018	0.33	95	1.3648	3.6	118.7
s21e10m193v10	21.0	1.0	1.93	10000	13.00	2.91	10.08	620	1504	1681	7057	4457	1.02	93	1.8227	2.2	93.3
s21e10m193v20	21.0	1.0	1.93	20000	13.00	2.10	10.90	755	1669	1810	6796	4344	1.02	90	2.3857	2.3	91.8
s21e30m193v10	21.0	3.0	1.93	10000	13.00	2.50	10.49	1022	2645	2887	11879	6063	2.99	92	2.1063	1.3	78.4
s21e30m193v20	21.0	3.0	1.93	20000	13.00	2.07	10.92	1284	2814	3011	11449	5713	3.01	90	2.4034	1.4	76.7
s22e01m169v10	22.0	0.1	1.69	10000	14.42	5.31	9.11	194	233	334	3270	2250	0.18	99	0.2893	5.0	166.8
s22e01m169v20	22.0	0.1	1.69	20000	14.42	5.28	9.13	186	256	363	3168	2166	0.17	99	0.3039	5.2	165.8
s22e03m169v10	22.0	0.3	1.69	10000	14.42	4.06	10.35	212	592	712	4177	2907	0.34	97	1.1604	3.9	130.9
s22e03m169v20	22.0	0.3	1.69	20000	14.42	3.41	11.01	230	646	758	4042	2838	0.32	96	1.6085	4.0	129.8
s22e10m169v10	22.0	1.0	1.69	10000	14.42	2.63	11.79	560	1353	1493	6848	4350	1.01	94	2.1420	2.4	101.8
s22e10m169v20	22.0	1.0	1.69	20000	14.42	1.85	12.56	678	1480	1595	6635	4263	1.01	91	2.5219	2.6	100.0
s22e30m169v10	22.0	3.0	1.69	10000	14.42	2.30	12.11	942	2362	2553	10974	6226	2.98	93	2.3654	1.4	85.4
s22e30m169v20	22.0	3.0	1.69	20000	14.42	1.79	12.62	1056	2482	2641	10701	5962	2.99	92	2.5332	1.5	83.4
s23e01m225v10	23.0	0.1	2.25	10000	13.00	5.91	7.09	342	462	662	4246	3109	0.30	98	0.2598	3.7	126.9
s23e01m225v20	23.0	0.1	2.25	20000	13.00	6.01	6.98	327	406	591	3919	2877	0.25	98	0.2060	4.0	130.0
s23e03m225v10	23.0	0.3	2.25	10000	13.00	5.51	7.49	302	694	917	5069	3600	0.45	97	0.5378	3.1	112.5
s23e03m225v20	23.0	0.3	2.25	20000	13.00	5.51	7.49	322	672	888	4742	3395	0.39	97	0.5378	3.4	116.1
s23e10m225v10	23.0	1.0	2.25	10000	13.00	3.99	9.01	620	1627	1873	7497	4830	1.08	93	1.6501	2.2	90.0
s23e10m225v20	23.0	1.0	2.25	20000	13.00	2.75	10.24	669	1803	1996	7070	4643	1.03	89	2.5469	2.3	90.9
s23e30m225v10	23.0	3.0	2.25	10000	13.00	3.22	9.77	1004	2931	3241	11857	6394	3.01	91	2.2039	1.3	75.4
s23e30m225v20	23.0	3.0	2.25	20000	13.00	2.53	10.46	1242	3229	3477	11306	6089	3.00	87	2.6748	1.5	74.2
s24e01m224v10	24.0	0.1	2.24	10000	14.01	6.15	7.85	329	419	583	4195	3139	0.32	98	0.2609	3.9	136.7
s24e01m224v20	24.0	0.1	2.24	20000	14.01	6.21	7.80	316	402	565	3813	2905	0.27	98	0.2309	4.2	143.3
s24e03m224v10	24.0	0.3	2.24	10000	14.01	5.82	8.19	364	583	780	4950	3625	0.47	98	0.4783	3.3	123.5
s24e03m224v20	24.0	0.3	2.24	20000	14.01	5.76	8.25	304	546	731	4578	3393	0.39	98	0.5210	3.6	127.2
s24e10m224v10	24.0	1.0	2.24	10000	14.01	4.29	9.72	476	1425	1649	7259	4877	1.08	95	1.5768	2.3	97.0
s24e10m224v20	24.0	1.0	2.24	20000	14.01	2.74	11.27	538	1618	1791	6742	4657	1.01	91	2.6075	2.5	98.2
s24e30m224v10	24.0	3.0	2.24	10000	14.01	3.41	10.60	897	2651	2931	11520	6705	3.00	92	2.1847	1.4	80.7
s24e30m224v20	24.0	3.0	2.24	20000	14.01	2.52	11.49	1161	2948	3165	10943	6438	2.99	89	2.7279	1.6	79.3
s25e01m207v10	25.0	0.1	2.07	10000	12.53	6.69	5.84	370	607	926	4380	3221	0.28	96	0.2789	3.6	109.6
s25e01m207v20	25.0	0.1	2.07	20000	12.53	6.75	5.78	357	544	848	4045	3016	0.24	97	0.2447	3.9	112.7
s25e03m207v10	25.0	0.3	2.07	10000	12.53	6.24	6.28	322	916	1249	5272	3723	0.42	95	0.5821	3.1	98.9
s25e03m207v20	25.0	0.3	2.07	20000	12.53	6.15	6.38	278	873	1182	4881	3511	0.36	95	0.6522	3.3	101.7
s25e10m207v10	25.0	1.0	2.07	10000	12.53	4.15	8.38	661	2035	2357	7629	5073	1.03	88	2.0526	2.2	82.2
s25e10m207v20	25.0	1.0	2.07	20000	12.53	2.39	10.14	704	2189	2442	7238	4891	1.01	81	3.2101	2.3	84.9
s25e30m207v10	25.0	3.0	2.07	10000	12.53	3.23	9.30	899	3640	4054	11906	5954	2.98	85	2.6585	1.3	67.8
s25e30m207v20	25.0	3.0	2.07	20000	12.53	2.26	10.27	1165	3990	4308	11197	5720	2.98	77	3.2966	1.5	67.7

Table 5. Same as Table 2, but now for the non-rotating pre-SN models of WHW02 with a main-sequence mass in the range 26–30 M_{\odot}

Simulation Name	M_i [M_{\odot}]	E_{kin} [B]	M_{piston} [M_{\odot}]	V_{piston} [km s $^{-1}$]	M_f [M_{\odot}]	M_{remnant} [M_{\odot}]	M_{ejecta} [M_{\odot}]	V_{inner} [km s $^{-1}$]	$V_{\text{e,O}}$ [km s $^{-1}$]	$V_{\text{i,H}}$ [km s $^{-1}$]	$V_{\text{p,15d}}$ [km s $^{-1}$]	$V_{\text{p,50d}}$ [km s $^{-1}$]	ϵ_{kt} [B]	ϵ_{kFH} %	M_{O} [M_{\odot}]	t_{SBO} [d]	Δt_P [d]
s26e01m205v10	26.0	0.1	2.05	10000	12.94	6.98	5.96	427	697	972	4470	3337	0.31	96	0.3054	3.6	109.5
s26e01m205v20	26.0	0.1	2.05	20000	12.94	7.01	5.93	363	608	867	4094	3113	0.26	97	0.2894	3.9	113.6
s26e03m205v10	26.0	0.3	2.05	10000	12.94	6.55	6.40	363	975	1263	5328	3831	0.44	95	0.5957	3.1	99.8
s26e03m205v20	26.0	0.3	2.05	20000	12.94	6.44	6.51	273	929	1197	4948	3605	0.38	95	0.6825	3.3	102.5
s26e10m205v10	26.0	1.0	2.05	10000	12.94	4.45	8.49	616	2050	2335	7643	5219	1.05	88	2.1377	2.2	83.6
s26e10m205v20	26.0	1.0	2.05	20000	12.94	2.43	10.51	613	2178	2403	7176	5006	1.01	82	3.5132	2.4	87.3
s26e30m205v10	26.0	3.0	2.05	10000	12.94	3.39	9.56	882	3676	4035	11855	6369	2.99	85	2.9015	1.4	69.1
s26e30m205v20	26.0	3.0	2.05	20000	12.94	2.26	10.68	1098	3997	4269	11125	6060	2.97	77	3.5759	1.5	69.2
s27e01m180v10	27.0	0.1	1.80	10000	12.45	7.30	5.15	333	1129	1162	4406	3234	0.26	94	0.3969	3.5	96.7
s27e01m180v20	27.0	0.1	1.80	20000	12.45	7.35	5.10	359	1071	1106	4130	3085	0.23	94	0.3849	3.7	99.1
s27e03m180v10	27.0	0.3	1.80	10000	12.45	6.73	5.72	458	1486	1528	5339	3776	0.40	92	0.7827	3.0	88.7
s27e03m180v20	27.0	0.3	1.80	20000	12.45	6.48	5.97	368	1433	1473	5009	3621	0.36	91	0.9704	3.2	90.8
s27e10m180v10	27.0	1.0	1.80	10000	12.45	3.81	8.64	586	2704	2747	7517	5010	1.01	81	2.8455	2.1	77.3
s27e10m180v20	27.0	1.0	1.80	20000	12.45	2.02	10.42	632	2722	2759	7155	4914	0.99	74	3.9244	2.3	79.4
s27e30m180v10	27.0	3.0	1.80	10000	12.45	2.86	9.59	784	4677	4737	11976	5184	2.96	77	3.5072	1.3	62.2
s27e30m180v20	27.0	3.0	1.80	20000	12.45	1.93	10.52	1141	4804	4851	11233	5066	2.97	68	3.9604	1.5	64.4
s28e01m180v10	28.0	0.1	1.80	10000	12.67	7.60	5.07	390	931	1241	4403	3270	0.27	94	0.3956	3.6	96.2
s28e01m180v20	28.0	0.1	1.80	20000	12.67	7.61	5.06	314	844	1149	4078	3086	0.23	94	0.3855	3.8	98.7
s28e03m180v10	28.0	0.3	1.80	10000	12.67	6.98	5.69	456	1304	1606	5258	3832	0.40	91	0.8294	3.0	87.5
s28e03m180v20	28.0	0.3	1.80	20000	12.67	6.82	5.85	428	1254	1536	4936	3646	0.36	91	0.9564	3.2	90.4
s28e10m180v10	28.0	1.0	1.80	10000	12.67	4.05	8.62	540	2534	2820	7603	5139	1.01	80	2.8917	2.2	76.8
s28e10m180v20	28.0	1.0	1.80	20000	12.67	2.04	10.63	590	2576	2813	7242	4989	1.00	73	4.1322	2.3	79.3
s28e30m180v10	28.0	3.0	1.80	10000	12.67	3.06	9.61	784	4467	4852	11956	5240	2.96	76	3.5817	1.4	62.0
s28e30m180v20	28.0	3.0	1.80	20000	12.67	1.93	10.74	922	4634	4922	11232	5064	2.97	67	4.1690	1.5	64.6
s29e01m172v10	29.0	0.1	1.72	10000	12.61	7.65	4.96	381	1176	1195	4742	2935	0.25	93	0.5331	3.3	89.9
s29e01m172v20	29.0	0.1	1.72	20000	12.61	7.71	4.90	390	1119	1139	4799	2839	0.23	93	0.5164	3.4	93.2
s29e03m172v10	29.0	0.3	1.72	10000	12.61	6.66	5.95	439	1557	1585	5571	3393	0.38	90	1.2387	2.8	84.8
s29e03m172v20	29.0	0.3	1.72	20000	12.61	6.47	6.14	395	1494	1520	5337	3283	0.35	89	1.3702	2.9	87.8
s29e10m172v10	29.0	1.0	1.72	10000	12.61	3.50	9.11	543	2815	2844	7722	4252	1.02	76	3.4100	2.0	72.9
s29e10m172v20	29.0	1.0	1.72	20000	12.61	1.98	10.63	671	2812	2838	7333	4193	1.01	70	4.4616	2.1	74.1
s29e30m172v10	29.0	3.0	1.72	10000	12.61	2.70	9.91	747	4820	4857	11867	2999	2.98	73	3.9617	1.2	58.7
s29e30m172v20	29.0	3.0	1.72	20000	12.61	1.90	10.71	1175	4876	4909	11079	3256	2.99	64	4.5272	1.3	60.5
s30e01m183v10	30.0	0.1	1.83	10000	12.24	8.04	4.20	596	1270	1572	4669	2668	0.25	88	0.6684	2.7	75.5
s30e01m183v20	30.0	0.1	1.83	20000	12.24	8.06	4.18	581	1201	1491	4433	2666	0.23	88	0.6536	2.9	77.5
s30e03m183v10	30.0	0.3	1.83	10000	12.24	6.86	5.38	512	1733	2017	5518	2722	0.39	83	1.5118	2.3	71.6
s30e03m183v20	30.0	0.3	1.83	20000	12.24	6.26	5.98	325	1677	1934	5254	2720	0.35	81	1.9286	2.5	73.7
s30e10m183v10	30.0	1.0	1.83	10000	12.24	3.74	8.50	516	3018	3307	7792	2128	1.02	68	3.6707	1.7	62.8
s30e10m183v20	30.0	1.0	1.83	20000	12.24	2.11	10.13	626	2975	3215	7420	2501	1.01	61	4.8107	1.8	63.8
s30e30m183v10	30.0	3.0	1.83	10000	12.24	3.02	9.22	687	5190	5588	12431	488	2.98	65	4.1709	1.0	52.8
s30e30m183v20	30.0	3.0	1.83	20000	12.24	2.07	10.17	1190	5159	5482	11436	1734	2.99	55	4.8369	1.2	54.8

Table 6. Same as Table 2, but now for our VID simulations based on the *rotating* pre-SN models E10, E12, E15, and E20 of HLW00.

Simulation Name	M_i [M_\odot]	E_{kin} [B]	M_{piston} [M_\odot]	V_{piston} [km s $^{-1}$]	M_f [M_\odot]	M_{remnant} [M_\odot]	M_{ejecta} [M_\odot]	V_{inner} [km s $^{-1}$]	$V_{\text{e,O}}$ [km s $^{-1}$]	$V_{\text{i,H}}$ [km s $^{-1}$]	$V_{\text{p,15d}}$ [km s $^{-1}$]	$V_{\text{p,50d}}$ [km s $^{-1}$]	ϵ_{kt} [B]	ϵ_{kfH} %	M_{O} [M_\odot]	t_{SBO} [d]	Δt_P [d]
E10e01m147v10	10.0	0.1	1.47	10000	9.23	1.80	7.42	195	129	354	3662	1625	0.15	99	0.0850	2.2	108.6
E10e01m147v20	10.0	0.1	1.47	20000	9.23	1.60	7.63	148	162	373	3483	1558	0.14	99	0.2379	2.4	123.5
E10e03m147v10	10.0	0.3	1.47	10000	9.23	1.61	7.61	281	320	567	5371	2209	0.34	99	0.2244	1.5	104.1
E10e03m147v20	10.0	0.3	1.47	20000	9.23	1.55	7.67	277	326	573	5359	2213	0.34	99	0.2697	1.5	104.7
E10e10m147v10	10.0	1.0	1.47	10000	9.23	1.47	7.75	310	424	963	8849	3202	1.00	99	0.3284	0.9	84.1
E10e10m147v20	10.0	1.0	1.47	20000	9.23	1.53	7.69	487	610	1016	8932	3268	1.04	99	0.2867	0.9	85.8
E10e30m147v10	10.0	3.0	1.47	10000	9.23	1.47	7.75	526	699	1436	14907	3439	3.02	99	0.3284	0.5	67.0
E10e30m147v20	10.0	3.0	1.47	20000	9.23	1.47	7.75	633	883	1678	14566	3995	3.03	99	0.3284	0.5	70.3
E12e01m160v10	12.0	0.1	1.60	10000	10.35	2.57	7.77	111	263	288	3098	1649	0.13	99	0.1020	3.4	116.9
E12e01m160v20	12.0	0.1	1.60	20000	10.35	2.38	7.96	151	130	301	2982	1591	0.12	99	0.1512	3.6	121.5
E12e03m160v10	12.0	0.3	1.60	10000	10.35	1.97	8.37	218	360	604	4689	2355	0.32	98	0.4336	2.3	116.6
E12e03m160v20	12.0	0.3	1.60	20000	10.35	1.66	8.68	245	463	677	4558	2343	0.31	98	0.6323	2.3	112.3
E12e10m160v10	12.0	1.0	1.60	10000	10.35	1.77	8.58	461	775	1163	8246	3656	1.01	98	0.5667	1.3	90.2
E12e10m160v20	12.0	1.0	1.60	20000	10.35	1.63	8.71	453	866	1200	8298	3612	1.01	98	0.6507	1.3	89.6
E12e30m160v10	12.0	3.0	1.60	10000	10.35	1.60	8.74	739	1283	1774	13656	4454	3.00	98	0.6696	0.8	72.8
E12e30m160v20	12.0	3.0	1.60	20000	10.35	1.62	8.72	776	1511	2053	13587	4847	3.01	98	0.6576	0.8	74.1
E15e01m176v10	15.0	0.1	1.76	10000	10.86	3.72	7.13	216	401	416	3791	2119	0.17	99	0.2181	4.0	137.6
E15e01m176v20	15.0	0.1	1.76	20000	10.86	3.72	7.13	200	382	397	3583	2021	0.16	99	0.2181	4.2	140.5
E15e03m176v10	15.0	0.3	1.76	10000	10.86	3.00	7.86	266	764	785	5199	2761	0.34	97	0.6736	3.0	112.2
E15e03m176v20	15.0	0.3	1.76	20000	10.86	2.43	8.43	344	843	861	4950	2679	0.32	96	1.0546	3.1	111.0
E15e10m176v10	15.0	1.0	1.76	10000	10.86	2.32	8.53	633	1575	1600	8125	4136	1.02	95	1.1224	1.8	87.3
E15e10m176v20	15.0	1.0	1.76	20000	10.86	1.88	8.98	720	1701	1725	7909	4018	1.01	93	1.3826	1.9	84.9
E15e30m176v10	15.0	3.0	1.76	10000	10.86	1.95	8.91	1170	2954	2987	12970	5341	2.99	93	1.3543	1.1	70.7
E15e30m176v20	15.0	3.0	1.76	20000	10.86	1.85	9.01	1191	2900	2930	12960	5167	3.01	93	1.3963	1.1	71.1
E20e01m200v10	20.0	0.1	2.00	10000	11.01	5.73	5.27	590	1331	1350	4221	3216	0.25	89	0.9298	5.5	94.5
E20e01m200v20	20.0	0.1	2.00	20000	11.01	6.70	4.31	640	867	892	3847	2910	0.21	96	0.4812	5.9	102.8
E20e03m200v10	20.0	0.3	2.00	10000	11.01	6.70	4.31	732	1020	1049	5076	3772	0.36	97	0.4812	4.6	92.6
E20e03m200v20	20.0	0.3	2.00	20000	11.01	5.18	5.83	659	1658	1680	4834	3754	0.36	86	1.1881	4.8	88.8
E20e10m200v10	20.0	1.0	2.00	10000	11.01	6.70	4.31	1037	1430	1467	7054	5387	0.78	97	0.4812	3.1	80.4
E20e10m200v20	20.0	1.0	2.00	20000	11.01	2.45	8.56	534	2778	2810	6861	5580	0.99	77	3.0123	3.3	76.3
E20e30m200v10	20.0	3.0	2.00	10000	11.01	2.76	8.25	1047	4735	4784	11752	5829	2.94	78	2.8142	1.9	61.7
E20e30m200v20	20.0	3.0	2.00	20000	11.01	2.24	8.76	1258	4792	4836	11249	5736	2.94	72	3.1634	2.1	63.2